ARTICLES
https://doi.org/10.1038/s41591-021-01323-8

nature medicine

Check for updates

A single-cell map of intratumoral changes during anti-PD1 treatment of patients with breast cancer

Ayse Bassez[1,2,10], Hanne Vos[3,10], Laurien Van Dyck[1,2], Giuseppe Floris[4], Ingrid Arijs[1,2], Christine Desmedt[5], Bram Boeckx[1,2], Marlies Vanden Bempt[2], Ines Nevelsteen[3], Kathleen Lambein[3], Kevin Punie[6], Patrick Neven[7], Abhishek D. Garg[8], Hans Wildiers[6], Junbin Qian[9]✉, Ann Smeets[3]✉ and Diether Lambrechts[1,2]✉

Immune-checkpoint blockade (ICB) combined with neoadjuvant chemotherapy improves pathological complete response in breast cancer. To understand why only a subset of tumors respond to ICB, patients with hormone receptor-positive or triple-negative breast cancer were treated with anti-PD1 before surgery. Paired pre- versus on-treatment biopsies from treatment-naive patients receiving anti-PD1 ($n=29$) or patients receiving neoadjuvant chemotherapy before anti-PD1 ($n=11$) were subjected to single-cell transcriptome, T cell receptor and proteome profiling. One-third of tumors contained *PD1*-expressing T cells, which clonally expanded upon anti-PD1 treatment, irrespective of tumor subtype. Expansion mainly involved CD8$^+$ T cells with pronounced expression of cytotoxic-activity (*PRF1*, *GZMB*), immune-cell homing (*CXCL13*) and exhaustion markers (*HAVCR2*, *LAG3*), and CD4$^+$ T cells characterized by expression of T-helper-1 (*IFNG*) and follicular-helper (*BCL6*, *CXCR5*) markers. In pre-treatment biopsies, the relative frequency of immunoregulatory dendritic cells (*PD-L1*$^+$), specific macrophage phenotypes (*CCR2*$^+$ or *MMP9*$^+$) and cancer cells exhibiting major histocompatibility complex class I/II expression correlated positively with T cell expansion. Conversely, undifferentiated pre-effector/memory T cells (*TCF7*$^+$, *GZMK*$^+$) or inhibitory macrophages (*CX3CR1*$^+$, *C3*$^+$) were inversely correlated with T cell expansion. Collectively, our data identify various immunophenotypes and associated gene sets that are positively or negatively correlated with T cell expansion following anti-PD1 treatment. We shed light on the heterogeneity in treatment response to anti-PD1 in breast cancer.

Triple-negative breast cancer (TNBC) comprises ~15% of all breast cancer (BC) patients and represents a heterogeneous group of tumors associated with poor outcome[1]. Of all BC subtypes, TNBC exhibits the highest number of tumor-infiltrating lymphocytes (TILs)[2,3], suggesting that TNBC could benefit from immune checkpoint blockade (ICB). The neutralizing PD-L1 antibody atezolizumab improves progression-free and overall survival when combined with nab-paclitaxel as first-line treatment in PD-L1$^+$ metastatic TNBC[4]. Anti-PD-L1 alone was also superior to maintenance chemotherapy in metastatic TNBC that was not progressive after six to eight cycles of chemotherapy[5]. Moreover, interim analysis of KEYNOTE-522, investigating the addition of an anti-PD1 antibody to neoadjuvant platinum-containing chemotherapy in previously untreated early TNBC, revealed an improvement in pathological complete response (pCR) rate and event-free survival[6]. ICB is also being explored as a neoadjuvant treatment for other BC subtypes (NCT03725059 or KEYNOTE-756 in estrogen receptor-positive (ER$^+$) and human epidermal growth factor receptor 2-negative (HER2$^-$) BC). This suggests that neoadjuvant ICB will soon become part of the standard of care for BC treatment.

However, not all BC patients respond to neoadjuvant ICB. An outstanding question is therefore to identify which underlying mechanisms and associated markers determine treatment response. So far, TIL scores and tumor PD-L1 expression have been proposed to predict clinical outcome[7,8], but their efficacies as predictive markers are still unclear. Indeed, TILs represent a heterogeneous population of cells with respect to cell type composition, gene expression and functional properties, and also differ between BC subtypes[3,9]. It is also not straightforward to delineate how TILs affect treatment outcome, as in the neoadjuvant setting ICB is combined with chemotherapy and the response to neoadjuvant chemotherapy itself depends on TILs[3].

In several other cancers, such as melanoma or lung cancer, clonal expansion of T cells underlies the treatment response to ICB[10–12]. Single-cell characterization of pre- and on-treatment biopsies has provided important insights into the patterns of T cell expansion and its underlying mechanisms[13,14]. However, these studies have so far only been performed on easy-to-biopsy cancer types, such as melanoma or basal/squamous cell skin carcinoma, profiling few patients ($n=11$) or focusing exclusively on CD45$^+$-immune cells. Therefore, to identify the mechanisms underlying the response to ICB specifically in BC, we treated 40 BC patients with neoadjuvant anti-PD1 and monitored intratumoral changes by subjecting matched pre- and on-treatment biopsies to single-cell transcriptome (scRNA-seq), T cell receptor (scTCR-seq) and combined transcriptome and proteome (CITE-seq) sequencing.

[1]Laboratory for Translational Genetics, Department of Human Genetics, KU Leuven, Leuven, Belgium. [2]VIB Center for Cancer Biology, Leuven, Belgium. [3]Department of Surgical Oncology, University Hospitals Leuven, KU Leuven, Leuven, Belgium. [4]Department of Imaging & Pathology, Laboratory of Translational Cell & Tissue Research and Department of Pathology, University Hospitals Leuven, KU Leuven, Leuven, Belgium. [5]Laboratory for Translational Breast Cancer Research, Department of Oncology, KU Leuven, Leuven, Belgium. [6]Department of General Medical Oncology, University Hospitals Leuven, KU Leuven, Leuven, Belgium. [7]Department of Gynaecology and Obstetrics, University Hospitals Leuven, KU Leuven, Leuven, Belgium. [8]Laboratory of Cell Stress & Immunity, Department of Cellular & Molecular Medicine, KU Leuven, Leuven, Belgium. [9]Department of Gynecologic Oncology, Women's Hospital, Zhejiang University School of Medicine, Hangzhou, China. [10]These authors contributed equally: Ayse Bassez, Hanne Vos. ✉e-mail: dr_qian@zju.edu.cn; Ann.Smeets@uzleuven.be; Diether.Lambrechts@vib-kuleuven.be

Results

Single-cell profiling before and during anti-PD1 treatment. We conducted a window-of-opportunity study (BioKey, NCT03197389) involving early-diagnosed BC. Briefly, one cohort of patients with non-metastatic, treatment-naive primary invasive carcinoma of the breast was treated with one dose of pembrolizumab (Keytruda or anti-PD1) approximately 9 ± 2 days before surgery (Fig. 1a and Methods). A second cohort of patients received neoadjuvant chemotherapy for 20–24 weeks, which was followed by pembrolizumab before surgery. In both cohorts, a tumor biopsy was collected immediately before anti-PD1 treatment ('pre-treatment'), while another biopsy was collected during subsequent surgery ('on-treatment'). Patients with different BC subtypes were included (Supplementary Tables 1 and 2 present the patient characteristics in both cohorts).

Using established protocols for scRNA-seq and scTCR-seq[15–17], we obtained high-quality data for 29 pairs of pre- and on-treatment biopsies from patients receiving only anti-PD1 (cohort 1). This involved 175,942 cells, with 1,759 genes per cell detected, on average (Supplementary Dataset 1). Subsequent analysis identified several clusters, which could be assigned to malignant breast epithelial cells, immune cells, endothelial cells and fibroblasts (Fig. 1b and Extended Data Fig. 1a,b). We confirmed that malignant breast epithelial clusters were copy number-unstable, while other cell populations, including fibroblasts, were copy number-stable (Extended Data Fig. 1c). Malignant cell clusters were patient-specific, while non-malignant clusters were shared between patients. There was no cluster bias in pre- versus on-treatment biopsies or different BC subtypes (Extended Data Fig. 1d–f).

We used scTCR-seq to define clonotypes based on shared TCR sequences in 51,499 T cells. As clonal thresholds, we considered T cells with shared sequences in >2 cells ($n = 12{,}531$) or >5 cells ($n = 7{,}793$). This identified nine patients with clonotype expansion on- versus pre-treatment at both thresholds (Fig. 1c). When considering clonotype proportions (clonotype frequencies normalized for the number of T cells), the same patients exhibited clonotype expansion. We designated these as patients with clonotype expansion or 'E(s)'. The other patients ($n = 20$) exhibited limited or no clonotype expansion and were designated 'NE(s)'. Some clonotypes also disappeared on-treatment, suggesting that T cells undergo 'clonotype contraction'. Clonotype contraction was less pronounced than clonotype expansion (Extended Data Fig. 2a,b), and was equally distributed between Es and NEs, suggesting it represents random sampling bias due to the comparison between biopsies taken from distinct tumor regions. Notably, some NEs ($n = 11$) exhibited a high percent of T cells before treatment (34.2 ± 3.8% versus 37.9 ± 5.7% in Es), but failed to expand upon anti-PD1. Other NEs ($n = 9$) represented cold tumors containing low T cell frequencies (8.4 ± 1.3%) and also failed to expand (Extended Data Fig. 2c). Finally, as much as 61% (range, 27–85%) of expanded T cells on-treatment had clonotypes already present pre-treatment (Extended Data Fig. 2d).

T cells expressing *PD1* proliferate after anti-PD1 treatment. Next, we analyzed scRNA-seq data while stratifying for T cell expansion (E versus NE) and treatment (pre- versus on-treatment). Pre-treatment, fibroblasts were more frequent in NEs, while T cells were more frequent in Es (Fig. 1d). On-treatment, cancer cells and fibroblasts were more frequent in NEs, while T cells were further enriched in Es (Fig. 1d). Indeed, the percent of stromal TILs determined either by immunohistochemistry or scRNA-seq increased on-treatment in Es (Extended Data Fig. 2e,f). Notably, tumor mutation burden and chromosomal instability did not differ between Es and NEs pre-treatment (Extended Data Fig. 2g,h).

PDCD1 (*PD1*) expression was limited to T cells and elevated in Es versus NEs, both pre- and on-treatment (Extended Data Fig. 2i,j). When subclustering T cells into their established phenotypes[16] (Fig. 1e and Extended Data Fig. 3a–c), we identified one CD8$^+$ and CD4$^+$ cluster expressing *PD1* (Fig. 1f and Extended Data Fig. 3b), representing activated T cells with exhaustion-like characteristics based on expression of immune-checkpoint (*LAG3*, *HAVCR2*, *PDCD1*), effector (*IFNG*, *NKG7*) and cytotoxic (*GZMB*, *PRF1*) markers. We refer to these as experienced T cells (T_{EX} cells). We also detected a third *PD1*$^+$ cluster consisting of highly proliferative T cells. Their relative abundance was higher in Es both pre- and on-treatment, but increased on-treatment (Fig. 1g). Proliferating T cells mainly consisted of CD8$^+$ and CD4$^+$ T_{EX} cells, although a subset (13%) represented CD4$^+$ regulatory T_{REG} cells (Extended Data Fig. 3d,e). Up to 59% of proliferating T cells also shared clonotypes with their non-proliferating CD4$^+$ and CD8$^+$ T_{EX} counterparts. We therefore assigned proliferating T cells to their respective CD8$^+$ T_{EX}, CD4$^+$ T_{EX} and T_{REG} subclusters (Extended Data Fig. 3f). The resulting subclusters of CD4$^+$ and CD8$^+$ T_{EX} cells were more frequent pre-treatment in Es than in NEs (Fig. 1h and Extended Data Fig. 3g). On-treatment, expanded T cells mainly comprised CD4$^+$ and CD8$^+$ T_{EX} cells, although a subset represented CD8$^+$ effector/memory T cells (T_{EM} cells; Extended Data Fig. 3h).

The T cell clonality and Gini index were increased in Es versus NEs both pre- and on-treatment, with the highest clonality observed in T_{EX} cells (Extended Data Fig. 3i). Conversely, clonotype richness was lower in Es than in NEs, pre- and on-treatment (Fig. 1i). When assessing whether pre-treatment *PD1*, T_{EX} cell abundance, T cell clonality and richness could predict T cell expansion, we obtained area under the curve (AUC) values that were considerably better compared to the TIL scores, the number of T cells or tumor mutation burden (0.92–0.96 versus 0.57–0.76; Extended Data Fig. 3j and Supplementary Dataset 2). We confirmed increased PD1 expression in pre-treatment T cells from Es using CITE-seq (Fig. 1j). Collectively, these data suggest that the % of PD1$^+$ T cells, rather than the % of all T cells or TILs, is associated with T cell expansion, and that CD8$^+$ and CD4$^+$ T_{EX} cells represent the majority of expanding T cells following anti-PD1.

Fig. 1 | BioKey study design and annotation of cell and T cell phenotypes by scRNA-seq. a, Design of the BioKey study in treatment-naive BC patients receiving one dose of anti-PD1. **b**, Uniform Manifold Approximation and Projection (UMAP) map of 175,942 cells color-coded for the indicated cell type. pDC, plasmacytoid dendritic cell. **c**, Number of expanded clonotypes in on- versus pre-treatment biopsies using three definitions (Methods). Prop, proportion; freq, frequency (see main text). **d**, Relative contribution of each cell type (in %) pre- (upper) and on-treatment (lower), comparing Es (patients with clonotype expansion, $n = 9$) versus NEs (patients with limited or no clonotype expansion, $n = 20$). **e**, Subclustering of T/natural killer (NK) cells into 14 phenotypes, as indicated by the color-coded legend. We identified naive (CD4$^+$ and CD8$^+$ T_N), regulatory (CD4$^+$ T_{REG}), effector/memory (CD4$^+$ and CD8$^+$ T_{EM}), recently activated effector/memory (CD8$^+$ T_{EMRA}), tissue-resident memory (CD8$^+$ T_{RM}), experienced (CD4$^+$ and CD8$^+$ T_{EX}) and proliferating T cells. We identified gamma-delta (γδ) T cell clusters with semi-invariant T cell repertoires (Vγ9/Vδ2 Tγδ) and with memory features (Tγδ). Two clusters represent resting and cytotoxic NK cells (NK_{rest} and NK_{cyto} cells). **f**, Heatmap of normalized *PD1* expression in T/NK cell phenotypes. **g**, Percentage of proliferating T cells (relative to all T cells), comparing Es ($n = 9$) with NEs ($n = 20$), pre- and on-treatment. **h**, Relative contribution of each T cell phenotype (in %) pre-treatment comparing Es ($n = 9$) with NEs ($n = 20$). **i**, TCR richness comparing Es ($n = 9$) with NEs ($n = 20$), pre- and on-treatment. **j**, Violin plots of PD1 expression by CITE-seq. In **d** and **g**–**i**, exact *P* values by two-sided Mann–Whitney test or two-sided Wilcoxon matched-pairs signed rank test for paired samples (pre- versus on-treatment): $^*P < 0.05$, $^{**}P < 0.01$, $^{***}P < 0.001$. In **j**, $^{***}P < 0.001$ by two-sided Wilcoxon rank sum test and Bonferroni-corrected (Seurat). In **d** and **g**–**i**, boxes indicate median ± interquartile range; whiskers show minima and maxima.

T cell expansion along the CD8⁺ T_{EX} cell trajectory. Next, we generated computationally imputed pseudotime trajectories using Slingshot[18]. TCR richness was highest for CD8⁺ naive T cells (T_N cells; Extended Data Fig. 4a), which we considered the root of the trajectories. Similar to others[19], we observed three distinct CD8⁺ T cell trajectories (Fig. 2a): T_N were connected to T_{EM} cells,

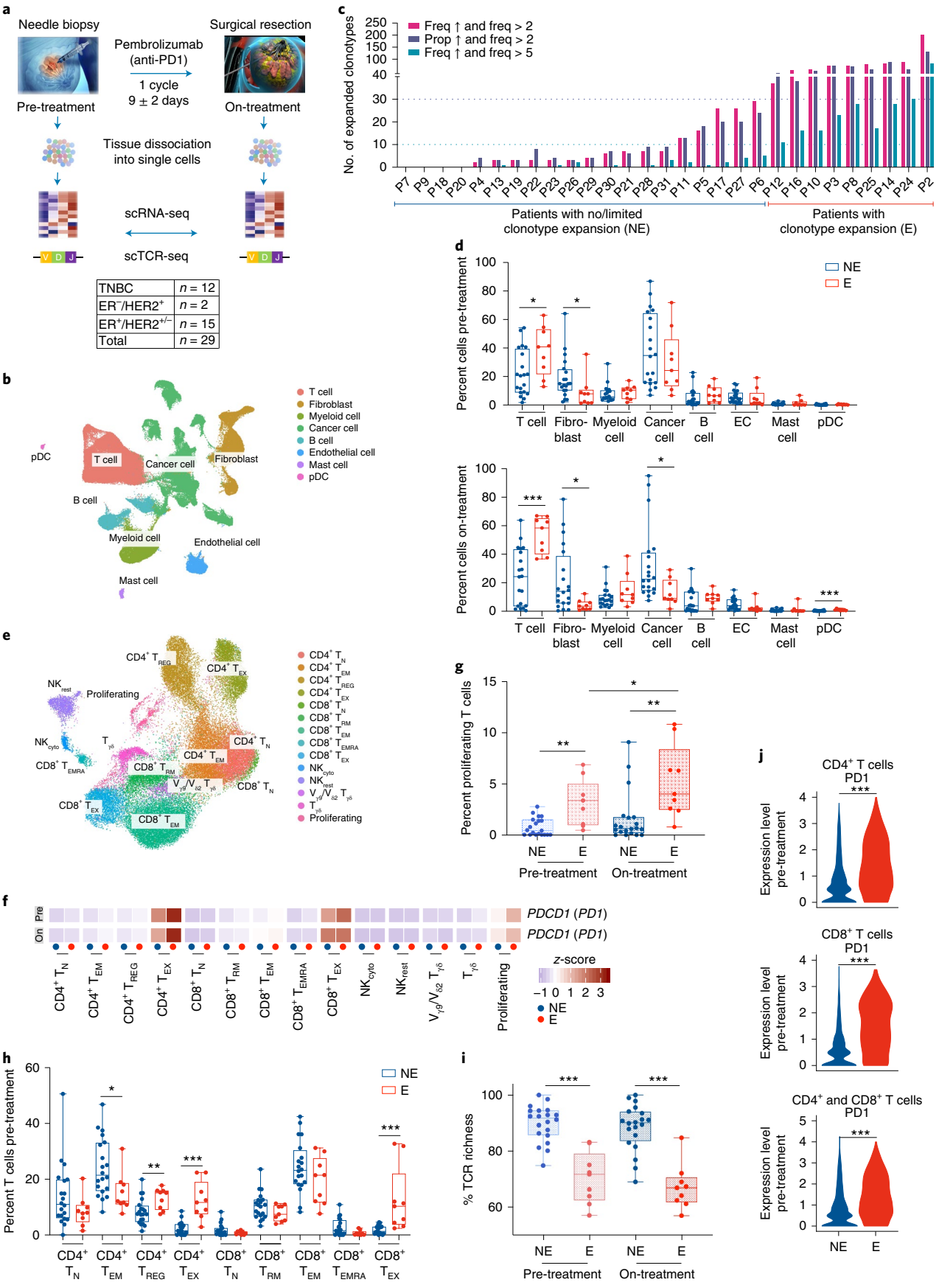

which branched into three different trajectories to form T_{EX1} and T_{EX2} cells, resident-memory CD8$^+$ T cells (T_{RM}) and activated effector/memory T cells (T_{EMRA} cells)[19]. TCR richness decreased along the trajectories, and clonotypes were often shared between subsequent T cell phenotypes (Fig. 2b and Extended Data Fig. 4a,b). RNA velocity analysis confirmed these trajectories, while profiling of marker genes confirmed their functional annotation (Fig. 2c,d and Extended Data Fig. 4c). T_{EX} cells were more frequent at the end of the trajectory in Es versus NEs, both pre- and on-treatment (Fig. 2e and Extended Data Fig. 4d). The difference was more pronounced on- versus pre-treatment in Es. Consequently, T_{EX} cells from Es on-treatment were characterized by more 'pronounced effector activity' and 'transient/early exhaustion' (Extended Data Fig. 4e). Increased cytotoxicity in Es was confirmed by CITE-seq based on expression of LAMP1, a marker of T cell degranulation (Extended Data Fig. 4f)[20]. In NEs, T_{EM} cells mainly resided midway in the trajectory, suggesting T cell effector function ablation in NEs.

TCR richness was lower in Es than in NEs in all trajectories (Fig. 2e). Along the T_{RM} and T_{EMRA} trajectories there was no decrease in richness, while along the T_{EX} trajectory richness decreased, particularly in Es. Moreover, decreases were more pronounced on- versus pre-treatment, reflecting ongoing T cell expansion induced by anti-PD1. Cell cycle scores also increased along the T_{EX} trajectory in Es and were higher on- versus pre-treatment, especially at the end (Extended Data Fig. 4g). Finally, we discerned expanding versus non-expanding T cells (irrespective of their E or NE status) along the trajectories (Fig. 2e). This confirmed that expanding T_{EX} cells were enriched towards the end of the trajectory, especially on-treatment.

T cell expansion along CD4$^+$ T_{H1} and T_{FH} cell trajectories. In CD4$^+$ T cells (T_{REG} excluded), additional phenotypic heterogeneity was identified with Slingshot. Experienced T_{EX} cells were split into type-1 helper (T_{H1}) and follicular helper (T_{FH}) cells (Fig. 2f and Extended Data Fig. 4h). Although immune-checkpoint markers (*PDCD1*, *CTLA4*) were highly expressed in both T_{H1} and T_{FH} cells, they differed in the expression of T_{H1}- (*IFNG*, *GZMB*) and T_{FH}-specific (*BCL6*, *CXCR5*) markers. Slingshot identified a trajectory starting in T_{N1} cells, progressing towards T_{N2} cells, followed by $T_{EM1–3}$ cells, then separating into trajectories involving either T_{H1} or T_{FH} cells. Clonotype sharing was highest between subsequent phenotypes, while RNA velocity independently confirmed these trajectories (Fig. 2g,h and Extended Data Fig. 4i,j). Profiling of marker genes and related TFs along trajectories confirmed their functional annotation (Fig. 2i). T_{H1} and T_{FH} cells in NEs remained in early pre-effector/memory states, both pre- and on-treatment treatment (Fig. 2j and Extended Data Fig. 4k). By contrast, in Es they both accumulated at the end of the trajectory. Consequently, expression of T cell activity and early exhaustion markers were increased in T_{H1} and T_{FH} cells from Es on-treatment (Extended Data Fig. 4l). TCR richness decreased towards the end of the trajectories (Fig. 2j), especially in T_{H1} cells from Es, while proliferation increased towards the end of the trajectory in Es on-treatment (Extended Data Fig. 4m). When comparing expanding versus non-expanding CD4$^+$ T cells along the trajectories, both T_{H1} and T_{FH} cells were strongly enriched towards the end of the trajectory, especially in Es on-treatment (Fig. 2j). Overall, these data indicate that T_{H1} and T_{FH} trajectories substantially contribute to clonotype expansion, suggesting they support the ongoing effector function of CD8$^+$ T_{EX} cells.

Gene expression changes during T cell expansion. We identified five sets of differentially expressed genes (DEGs) along the CD8$^+$ T_{EX} trajectory. A first set, consisting of naive T cell markers (*CCR7*, *LEF1*) decreased along the trajectory, while two sets, consisting of (early) activation genes (*GZMK*, *GZMM*, *GZMA*, *NKG7*), increased halfway through the trajectory, but then decreased. Two other sets increased towards the end of the trajectory and were characterized by effector (*IFNG*), cytotoxicity (*GZMB*, *PRF1*), early and general exhaustion (*PDCD1*, *CTLA4*, *ENTPD1*; Fig. 3a) markers. In each gene set, we identified several genes previously unidentified as T cell markers (for example, *INPP5F* and *GPR25* as differentiated T_{EX} markers, Fig. 3a). Although trajectories allocate cells with a similar expression to the same pseudotime, we observed that some genes were differentially expressed between E and NE trajectories. For example, effector and cytotoxic-activity-related genes (*PRF1*, *GZMB*, *IFNG*), *CTLA4* and *TOX2* were consistently higher in Es (Fig. 3b). TradeSeq identified 390 such DEGs (Supplementary Dataset 3), including *RUNX3* and its co-factor *CBFB*, which were decreased in NEs (Fig. 3b). Pathway analyses revealed upregulation of interferon (IFN) responses and downregulation of oxidative phosphorylation in Es (Fig. 3c,d). Along the CD4$^+$ T_{H1} trajectory, we similarly identified five gene sets (Fig. 3e) and 499 DEGs when comparing Es versus NEs (Supplementary Dataset 4), including potential T_{H1} markers such as *ZEB2* (Fig. 3f). Similar to CD8$^+$ T cells, *RUNX3* and *CBFB* were reduced in NEs, while IFN-α/γ responses were increased in Es (Fig. 3f–h). Hence, gene expression profiling along trajectories identified markers or pathways differentially expressed or activated between Es and NEs.

Expression signatures in T cells predict T cell expansion. We next identified DEGs between T cells that expand versus T cells that do not expand pre-treatment (Fig. 4a, Extended Data Fig. 5a,b and Supplementary Dataset 5). Non-expanding T cells were more naive (*LEF1*, *SELL*, *TCF7*), while expanding T cells exhibited high

Fig. 2 | Trajectory analysis of CD8$^+$ and CD4$^+$ T cells according to T cell expansion. a, Pseudotime trajectories for CD8$^+$ T cells based on Slingshot, showing three trajectories (T_{RM}, T_{EX} and T_{EMRA}), color-coded for CD8$^+$ T cell phenotypes (left), pseudotime (middle) and number of clonotypes detected (right). **b**, Barplot showing the shared TCR weight for the indicated CD8$^+$ T cell phenotype with all other phenotypes, illustrating that subsequent phenotypes share the most TCRs. **c**, RNA velocity analysis on CD8$^+$ T cell phenotypes independently confirming the three trajectories. **d**, Plot of marker and functional genes along the CD8$^+$ T cell trajectories. TF, transcription factor. **e**, Densities and clonotype richness along the CD8$^+$ trajectories pre- and on-treatment. The density plots reflect the relative number of T cells separately for E versus NE (upper) or the relative number of expanding versus non-expanding T cells (lower) along the CD8$^+$ trajectories, pre- and on-treatment. TCR clonotype richness (middle) along the CD8$^+$ trajectories is stratified for E versus NE. **f**, Pseudotime trajectories for CD4$^+$ T cells based on Slingshot, showing two trajectories (T_{H1}, T_{FH}), color-coded for CD4$^+$ T cell phenotypes (left), pseudotime (middle) and number of clonotypes detected (right). **g**, Barplot showing shared TCR weight for the indicated CD4$^+$ T cell phenotype with all other phenotypes. The high amount of TCR sharing observed between T_{H1} and T_{FH} cells could be due to type-conversion between both phenotypes or because they share common precursor cells. **h**, RNA velocity analysis on CD4$^+$ T cell phenotypes (excluding T_{REG}). **i**, Plot of marker and functional genes along the CD4$^+$ trajectories. **j**, Densities and TCR richness along the CD4$^+$ trajectories pre- and on-treatment. The density plots reflect the relative number of T cells separately for E versus NE (upper) or the relative number of expanding versus non-expanding T cells (lower) along the CD4$^+$ trajectories, pre- and on-treatment. TCR clonotype richness (middle) along the CD4$^+$ trajectories is stratified for E versus NE. *P* values assessing differences on- versus pre-treatment in pseudotime for CD8$^+$ T_{EX} cells, CD4$^+$ T_{H1} cells and CD4$^+$ T_{FH} cells in Es: $P = 2.5 \times 10^{-4}$, $P = 2.5 \times 10^{-14}$ and $P = 0.007$; in Es versus NEs, pre-treatment: $P = 8.8 \times 10^{-59}$, $P = 1.1 \times 10^{-28}$ and $P = 1.2 \times 10^{-21}$ and on-treatment: $P = 6.7 \times 10^{-39}$, $P = 2.2 \times 10^{-103}$ and $P = 5.5 \times 10^{-31}$. Gray shading in **d** and **i** represents 95% confidence intervals at any given pseudotime.

effector function (*IFNG*), immune cell-homing signals (*CXCL13*, *CCL3/4/5*), cytotoxicity (*GZMB*, *PRF1*, *NKG7*), antigen presentation (*CD74*, *HLA-DRB1/5*, *HLA-DQA2*) and immune-checkpoint marker expression (*PDCD1*, *HAVCR2*, *LAG3*). *ENTPD1* (*CD39*) and *ITGAE* (*CD103*), which mark tumor-reactive T cells[21,22], were also pronounced in expanding T cells. Gene set enrichment analysis

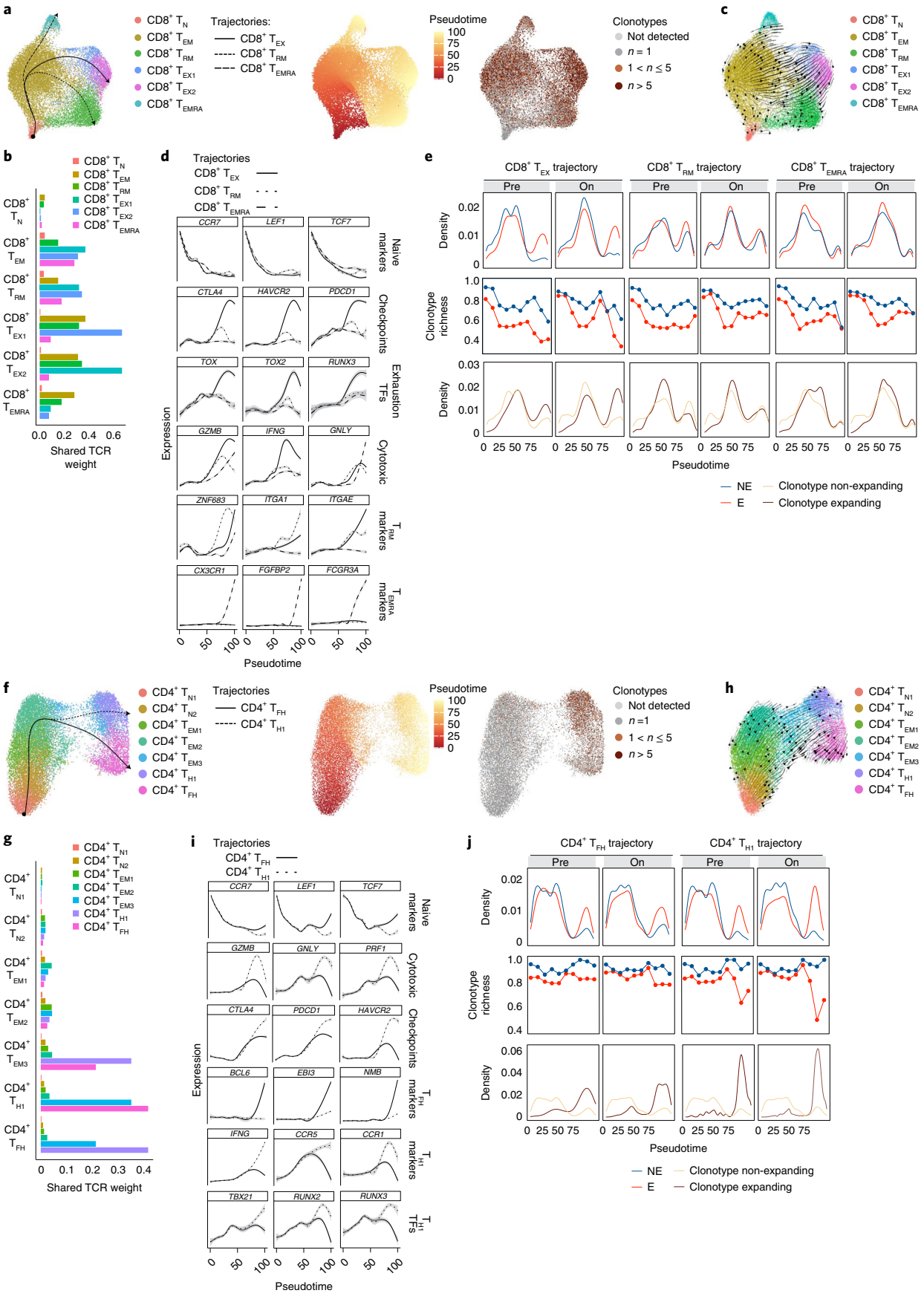

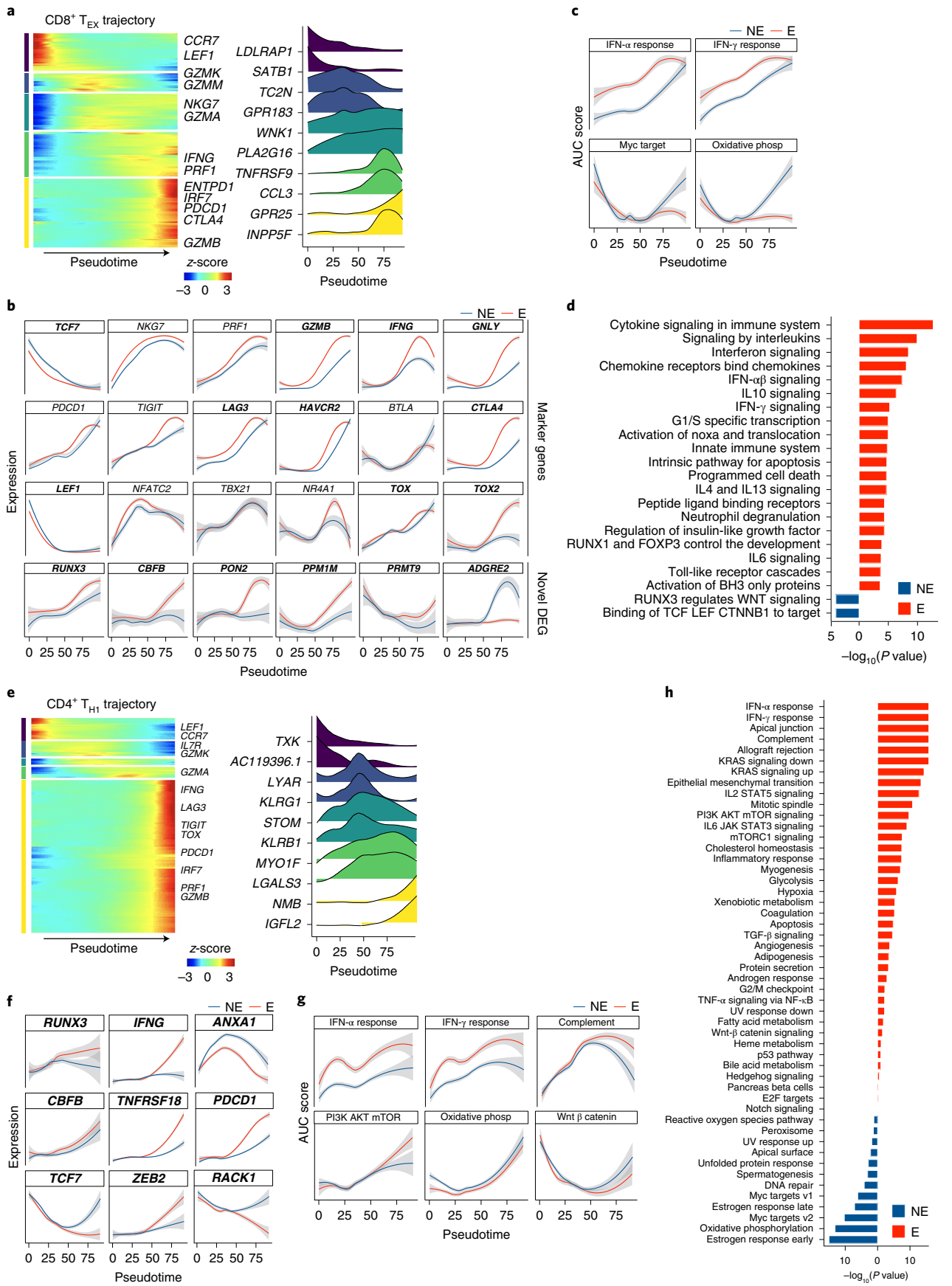

(GSEA) on DEGs confirmed these differences (Extended Data Fig. 5c,d). The number of expanded clonotypes (per patient) also correlated with expression of these genes or their associated pathways pre-treatment (Extended Data Fig. 5e and Supplementary Dataset 2). Immune-checkpoint markers and CD4$^+$ T_{H1} activity were most predictive for T cell expansion in Es versus NEs pre-treatment

Fig. 3 | Differentially expressed genes in CD8$^+$ T_{EX} and CD4$^+$ T_{H1} trajectories. a, Gene expression dynamics along the CD8$^+$ T_{EX} trajectory. Genes cluster into five gene sets, each characterized by specific expression profiles, as depicted by a selection of marker genes characteristic for each cluster (left). For each gene cluster (indicated by different colors), expression of two novel genes along the trajectory is shown (right). **b**, Plots showing the expression dynamics of 18 marker or functional genes (rows 1–3) and six DEGs previously not implicated in T cell biology and identified by TradeSeq (row 4) between Es and NEs pre-treatment along the trajectory. Marker genes that were differentially expressed by TradeSeq are indicated in bold. **c**, Plots showing hallmark pathway activity scores by AUCell along the CD8$^+$ T_{EX} trajectory comparing Es and NEs. **d**, GSEA on DEGs in Es versus NEs along the CD8$^+$ T_{EX} trajectory using hyperR for REACTOME and hallmark gene sets. **e**, Gene expression dynamics along the CD4$^+$ T_{H1} trajectory. Genes cluster into five gene sets, each characterized by specific expression profiles, as depicted by a selection of marker genes characteristic for each cluster (left). For each gene cluster (indicated by different colors), expression of two novel genes along the trajectory is shown (right). **f**, Plots showing nine DEGs previously not implicated in T cell biology and identified by TradeSeq between E and NEs along the CD4$^+$ T_{H1} trajectory. **g**, Plots showing hallmark pathway activity scores by AUCell along the CD4$^+$ T_{H1} trajectory comparing Es and NEs. **h**, GSEA on DEGs for Es versus NEs along the CD4$^+$ T_{H1} trajectory using hyperR for REACTOME and hallmark gene sets. Gray shading in **b**, **c**, **f** and **g** represents the 95% confidence interval at any given pseudotime.

(AUC = 0.93–0.96 versus 0.70–0.87 for CD8$^+$ cytotoxicity and IFN-γ activity; Fig. 4b). A signature of 50 DEGs in CD4$^+$ T cells for Es versus NEs pre-treatment similarly predicted T cell expansion (Supplementary Dataset 6 and Extended Data Fig. 5f). CITE-seq confirmed that naive T cell markers were higher in NEs than in Es, while immune-checkpoint, tumor-reactive and co-stimulatory markers were reduced (Fig. 4c and Extended Data Fig. 5g).

When comparing Es with TNBC ($n = 5$) versus ER$^+$ BC ($n = 3$), the number of expanded clonotypes did not differ. Nevertheless, pre-treatment *PD1* expression in T cells and the number of proliferating T cells were higher in TNBC (Fig. 4d,e and Extended Data Fig. 6a,b). Es also exhibited increased expression of CD8$^+$ T cell effector function genes, CD4$^+$ T_{H1} activity and immune-checkpoint genes pre-treatment in TNBC (Fig. 4f). DEGs in expanding CD8$^+$ T cells from TNBC versus ER$^+$ Es also revealed elevated effector function (Extended Data Fig. 6c), while in expanding CD4$^+$ T cells, expression of antigen presentation genes (*HLA-C*, *HLA-DRB5*), *GZMB* and *ENTPD1* was increased (Extended Data Fig. 6d). Conversely, in ER$^+$ Es, expanding CD4$^+$ and CD8$^+$ T cells overexpressed naive (*SELL*, *IL7R*) and pre-effector (*GZMK*) markers, suggesting that although the extent of T cell expansion was similar, they were less differentiated compared to TNBC.

T cell expansion after neoadjuvant chemotherapy and anti-PD1. Next, we analyzed pairs of pre- and on-treatment biopsies ($n = 11$) from patients receiving neoadjuvant chemotherapy before anti-PD1 (cohort 2). Using the same analysis strategy as in cohort 1, we designated three patients as Es (Fig. 4g and Extended Data Fig. 6e). T cells and pDCs were increased on-treatment, but not pre-treatment in Es, while *PD1* was increased both pre- and on-treatment in Es (Fig. 4h–i and Extended Data Fig. 6f,g). Subclustering of T cells confirmed that CD4$^+$ and CD8$^+$ T_{EX} cells were more frequent in Es, both pre- and on-treatment (Fig. 4j and Extended Data Fig. 6h). Comparing expanding and non-expanding T cells pre-treatment identified similar DEGs or pathways as in patients receiving only anti-PD1 (Extended Data Fig. 6i). The same genes or pathways also predicted T cell expansion (Supplementary Dataset 7). T_{H1} activity and our signature of 50 DEGs in T_{H1} cells reliably predicted T cell expansion (AUC = 0.958 and 0.917; Extended Data Fig. 6j), confirming that CD4$^+$ T_{H1} cells are also involved in T cell expansion when anti-PD1 is combined with neoadjuvant chemotherapy.

Dendritic cells associated with T cell expansion. Dendritic cells (DCs) play a central role in regulating the balance between CD8$^+$ T cell immunity and tolerance to tumor antigens[23]. We therefore subclustered 2,410 DCs from patients receiving only anti-PD1 ($n = 29$) to reveal six phenotypes, including conventional type 1 and 2 DCs (cDC1, cDC2), plasmacytoid DCs (pDC), Langerhans-like DCs (LanghDC), migratory DCs (migDC) and the recently described AXL$^+$SIGLEC6$^+$ DCs (ASDC)[24,25] (Fig. 5a and Extended Data Fig. 7a–c). MigDCs clustered in separate subpopulations: a transcriptionally active population expressing immunoregulatory molecules (mregDC[26]; *PD-L1*/*L2*) and a quiescent population expressing migratory marker genes (*CCR7*, *CCL19*; Extended Data Fig. 7d,e).

PD-L1 (*CD274*) and *PD-L2* (*PDCD1LG2*) were increased in DCs from Es versus NEs (Fig. 5b). Immunohistochemistry confirmed that PD-L1 was higher in Es, both pre- and on-treatment (Fig. 5c). Within the DC subtypes, *PD-L1* was uniquely expressed by mregDCs (Fig. 5d). Relative DC frequencies pre-treatment did not differ between Es and NEs, except for mregDCs, which were enriched in Es pre-treatment (Fig. 5e and Extended Data Fig. 7f). Pre-treatment DEGs in Es versus NEs revealed increased levels of genes involved in IFN responsiveness (*STAT1*[27], *IFI27*, *ISG20*), DC differentiation (*ETV6*[28]), antigen cross-presentation (HLA genes) and

Fig. 4 | Expanding versus non-expanding T cells in BC and in BC subtypes. a, Volcano plot showing DEGs in T cells comparing expanding ($n = 910$ cells) and non-expanding ($n = 16{,}144$ cells) T cells pre-treatment. Black dots on the volcano plot: P = NS (not significant); gray, $P < 0.05$; red, $P < 0.05$ and absolute $\log_2$FC ≥ 0.5 (FC, fold change). *P* values were obtained by the model-based analysis of single-cell transcriptomics (MAST) test and Bonferroni-corrected (Seurat). Genes in bold are discussed in the main text. **b**, Receiver operating characteristic (ROC) curves for eight genes (left) and six signature module scores (right), calculated based on scRNA-seq data comparing Es and NEs pre-treatment. AUC values and 95% confidence intervals indicating the predictive effect are indicated. **c**, Violin plots showing expression of the indicated proteins by CITE-seq, confirming differences observed by scRNA-seq. **d**, Number of expanded clonotypes in Es ($n = 8$) and NEs ($n = 19$) comparing ER$^+$ ($n = 15$; Es: $n = 3$) versus triple-negative breast cancer (TNBC, $n = 12$; Es: $n = 5$). No significant difference was observed between ER$^+$ Es and TNBC Es. **e**, Boxplot showing average *PD1* expression in T cells comparing ER$^+$ ($n = 3$) and TNBC ($n = 5$) Es pre-treatment. **f**, Boxplots showing average CD8$^+$ IFN-γ response signature, CD4$^+$ T_{H1} activity and CD4$^+$ immune-checkpoint module scores comparing ER$^+$ ($n = 3$) and TNBC ($n = 5$) Es pre-treatment. **g**, Number of expanded clonotypes in on- versus pre-treatment biopsies from 11 patients receiving neoadjuvant chemotherapy followed by a single dose of anti-PD1 (replication cohort or cohort 2) according to three definitions of expanded clonotypes. **h**, Relative contribution of each cell type (in %) in on-treatment biopsies within the replication cohort comparing Es ($n = 3$) and NEs ($n = 8$). **i**, Heatmap of normalized *PD1* expression (replication cohort) showing increased expression in Es, both pre- and on-treatment. **j**, Relative contribution of each T cell phenotype (in %) in pre-treatment biopsies (replication cohort) comparing Es ($n = 3$) and NEs ($n = 8$). In **d**–**f**, **h** and **j**, exact *P* values by Mann–Whitney test or Wilcoxon matched-pairs signed rank test for paired samples (pre- versus on-treatment) are shown (two-sided (**d**–**f**) or one-sided (**h**,**j**)): $^*P < 0.05$, $^{**}P < 0.01$, $^{***}P < 0.001$. In **c**, $^{***}P \leq 0.001$ by two-sided Wilcoxon rank sum test and Bonferroni-corrected (Seurat). In **d**–**f**, **h** and **j**, boxes indicate median ± interquartile range; whiskers indicate minima and maxima.

processing (*LY75*[29], *TAP1*[30]), and T cell co-stimulation (*CD80*) (Fig. 5f, Extended Data Fig. 7g and Supplementary Dataset 8). pDCs, ASDCs and mregDCs were more frequent in Es on-treatment (Fig. 5e,g). *CXCL9* and *CXCL10*, which are important for T cell migration towards the tumor[31], and genes associated with IFN responsiveness and antigen presentation were elevated in Es

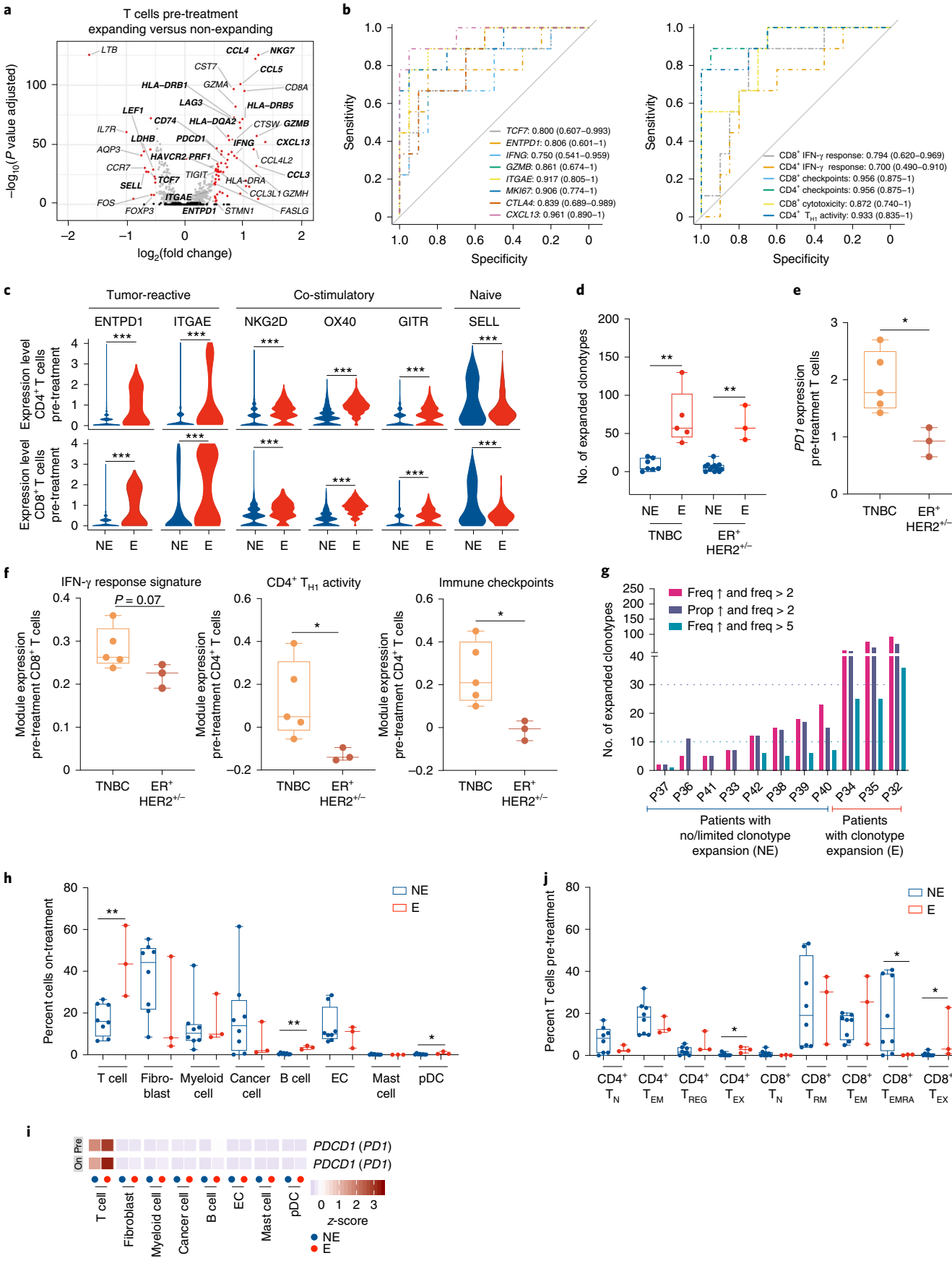

versus NEs on-treatment (Fig. 5f). Overall, this suggests that DCs are immunoresponsive in Es, both pre- and on-treatment, and support T cell function.

Macrophages expressing *PD-L1/L2* correlate with T cell expansion. Given that macrophages also act as mediators of tumor immunity, we subclustered the 7,952 myeloid cells into 10 pheno-

Fig. 5 | Dendritic cells and macrophages expressing PD-L1 correlate with T cell expansion. a, UMAP depicting six color-coded DC phenotypes. The migratory DCs could be further divided into two clusters of quiescent migDCs and mregDCs; the mregDC cluster is indicated with an arrow. **b**, Heatmap showing the expression of PD1 ligands (*PD-L1/L2*) in all cell types. Expression is highest in DCs, macrophages and monocytes in Es. **c**, Boxplot showing increased PD-L1 positivity based on immunohistochemistry as a modified proportion score (MPS) in Es ($n=8$) and NEs ($n=18$). **d**, Heatmap showing expression of PD1 ligands (*PD-L1/L2*) in all DC phenotypes. Expression is highest in mregDCs. **e**, Relative contribution of DCs (left) and mregDCs (right) to all cells (in %) both pre- and on-treatment, comparing Es ($n=9$) and NEs ($n=20$). **f**, Heatmap showing the expression of genes involved in IFN responsiveness (IFN-γ and IFN-α response genes), immune cell attraction, co-stimulation, antigen presentation and processing, and differentiation. **g**, Relative contribution of each DC phenotype (in %) to all cells on-treatment, comparing Es ($n=9$) and NEs ($n=20$). **h**, UMAP depicting 10 different myeloid cell phenotypes. **i**, Volcano plot showing DEGs in macrophages pre-treatment comparing Es and NEs. Black dots, $P=$ NS; gray, $P<0.05$; red, $P<0.05$ and absolute $\log_2$FC ≥ 0.5. *P* values were obtained by MAST test and are Bonferroni-corrected (Seurat). Genes in bold are discussed in this paper. **j**, Violin plots showing differential expression of the indicated proteins by CITE-seq in myeloid cells in Es and NEs pre-treatment. **k**, Heatmap showing expression of PD1 ligands (*PD-L1/L2*) in each monocyte and macrophage subcluster. **l**, Relative contribution of each myeloid cell phenotype (in %) in pre- (left) and on-treatment (right) biopsies comparing Es ($n=9$) and NEs ($n=20$). In **c**, **e**, **g** and **l**, exact *P* values by two-sided Mann–Whitney test or two-sided Wilcoxon matched-pairs signed rank test for paired samples (pre- versus on-treatment) are shown: $^{*}P<0.05$, $^{**}P<0.01$, $^{***}P<0.001$. In **j**, $^{**}P<0.01$, $^{***}P<0.001$ by two-sided Wilcoxon rank sum test and Bonferroni-corrected (Seurat). In **c**, **e**, **g** and **l**, boxes show the median ± interquartile range; whiskers indicate minima and maxima.

types, including two monocyte (C1 and C2) and eight macrophage (C3–C10) clusters (Fig. 5h). C1_CD14 monocytes represented classical monocytes (high *CD14*, *S100A8/9*), while the less-abundant C2_CD16 monocytes were non-classical (low *CD14*, high *FCGR3A* (CD16), *CDKN1C*, *MTSS1*) (Extended Data Fig. 7h–j). In addition to previously described macrophage phenotypes[16], we identified C7_MT1G macrophages (expressing metallothioneins regulating redox state[32]) and hypoxic C8_SLC2A1 macrophages.

Similar to DCs, macrophages expressed *PD-L1* and *PD-L2*. Macrophages were, however, more abundant than DCs (Extended Data Fig. 7k). In pre-treatment macrophages, *PD-L1/L2* was significantly higher in Es than in NEs (Fig. 5b), while several cytokines (*CXCL9*, *CXCL10*, *CCL8*) and type I/II IFN-responsive genes were upregulated (Fig. 5i, Extended Data Fig. 7l and Supplementary Dataset 9). By contrast, *CX3CR1* and *C3* were downregulated. CITE-seq confirmed increased expression of co-stimulatory markers in Es versus NEs pre-treatment (Fig. 5j). At the subcluster level, most macrophage phenotypes expressed *PD-L1* (Fig. 5k). C7_CX3CR1 macrophages were depleted in Es pre-treatment, an effect that became more pronounced on-treatment (Fig. 5l). By contrast, C3_CCR2 macrophages, which represent pro-inflammatory macrophages based on M1 marker expression (*CXCL9/10*, *SOCS3*), were enriched in Es on-treatment (Fig. 5l and Extended Data Fig. 7j).

Cancer cells are affected by anti-PD1 in tumors with T cell expansion. Because the activity of T cells relies on tumor antigen presentation by cancer cells, we also investigated the cancer cell compartment. Cancer cell numbers decreased on- versus pre-treatment in Es ($-16.83 \pm 6.67\%$; $P=0.039$ versus -6.53 ± 4.8 in NEs; $P=$ NS, Fig. 6a). Expression of the proliferation marker *MKI67* was also reduced by scRNA-seq, but this was not confirmed by Ki67 immunohistochemistry (Extended Data Fig. 8a). Although we failed to detect *PD-L1* in cancer cells, we observed that numerous antigen presentation major histocompatibility complex (MHC) class I/II genes were downregulated in NEs versus Es, both by scRNA-seq and CITE-seq (Fig. 6b,c). Pathways related to antigen processing or presentation, and IFN-γ response signaling, were upregulated in Es versus NEs pre-treatment (Extended Data Fig. 8b). Comparing Es pre- versus on-treatment confirmed an ongoing anti-tumor immune response, with cell proliferation, proteolysis, cell death, immune signaling and cytotoxicity pathways enriched in cancer cells from Es on-treatment (Fig. 6d and Extended Data Fig. 8c–f).

Immune environment associated with T cell expansion. Finally, we explored which cell types and phenotypes pre-treatment were correlated with T cell expansion. The relative frequency of $CD4^+$ or $CD8^+$ T_{EX} cells, proliferating T cells, migDCs, macrophage phenotypes expressing *PD-L1*, including $CCR2^+$ and $MMP9^+$ macrophages, correlated positively with T cell expansion. By contrast, naive or effector/memory T cells, and inhibitory ($CX3CR1^+$) macrophages, were inversely correlated (Fig. 6e). Similarly, pre-treatment expression of *PD1* in T cells, *PD-L1/2* in macrophages, MHC class I/II genes in cancer cells and T cell clonality correlated positively with T cell expansion, while *TCF7* and *SELL* in T cells, or *CX3CR1* and *C3* in macrophages, correlated inversely (Extended Data Fig. 9).

We also predicted receptor–ligand interactions using CellphoneDB[33]. First, we calculated the interactions between cell types separately for Es and NEs, both pre- and on-treatment (Extended Data Fig. 10a). We observed more interaction possibilities in Es than NEs pre-treatment, particularly between cancer cells, DCs, monocytes/macrophages and T cells (Fig. 6f and Extended Data Fig. 10b). Specific interactions between $CD8^+$ or $CD4^+$ T cells and other immune cells in Es included co-stimulatory (CD28-CD80, ICOS-ICOSLG) or co-inhibitory (PDCD1-CD274/PDCD1LG2 (PD1-PD-L1/2), HAVCR2-LGALS9 (TIM3-Galectin9), CTLA4-CD80/CD86) interactions (Fig. 6g,h and Supplementary Dataset 10). By contrast, $CD8^+$ T cells showed suppressive interactions with myeloid cells (LAIR1-LILRB4[34], TGFBR3-TGFB1[35]) and pro-apoptotic interactions (TNFSF10-TNFRSF10A) with monocytes/macrophages and cancer cells in NEs pre-treatment, while T cell homing interactions (CXCR3-CXCL9/CXCL10/CXCL11) were lacking (Fig. 6g and Extended Data Fig. 10c). On-treatment, we observed a significant reduction in the number of interactions between cancer cells and other cell types in Es (Extended Data Fig. 10d,e). Between cancer cells and $CD8^+$ T cells, several new interactions suggestive of T cell recruitment were observed in Es (CXCL10_CXCR3, ICAM1_LFA1), while co-stimulatory interactions (TNFRSF9-TNFSF9) were seen between $CD8^+$ T cells and DCs (Extended Data Fig. 10c,f). Overall, these data depict an interactive immune environment in pre-treatment biopsies that correlates with T cell expansion following anti-PD1 treatment.

Discussion

Here, we have unbiasedly assessed intratumoral changes in BC patients receiving ICB. Others have already characterized treatment-naive BC microenvironments at single-cell resolution[36–38]. By accurately monitoring how anti-PD1 affects immune cells and vice versa how immune cells pre-treatment correlate with T cell expansion, we complement these efforts in the context of ICB.

Because anti-PD1 was delivered in a window-of-opportunity setting, we could not explore whether T cell expansion translates into clinical benefit. However, in melanoma, peripheral T cell expansion occurring within three weeks after start of treatment correlates with improved clinical response to ICB six months later[39,40]. Because the

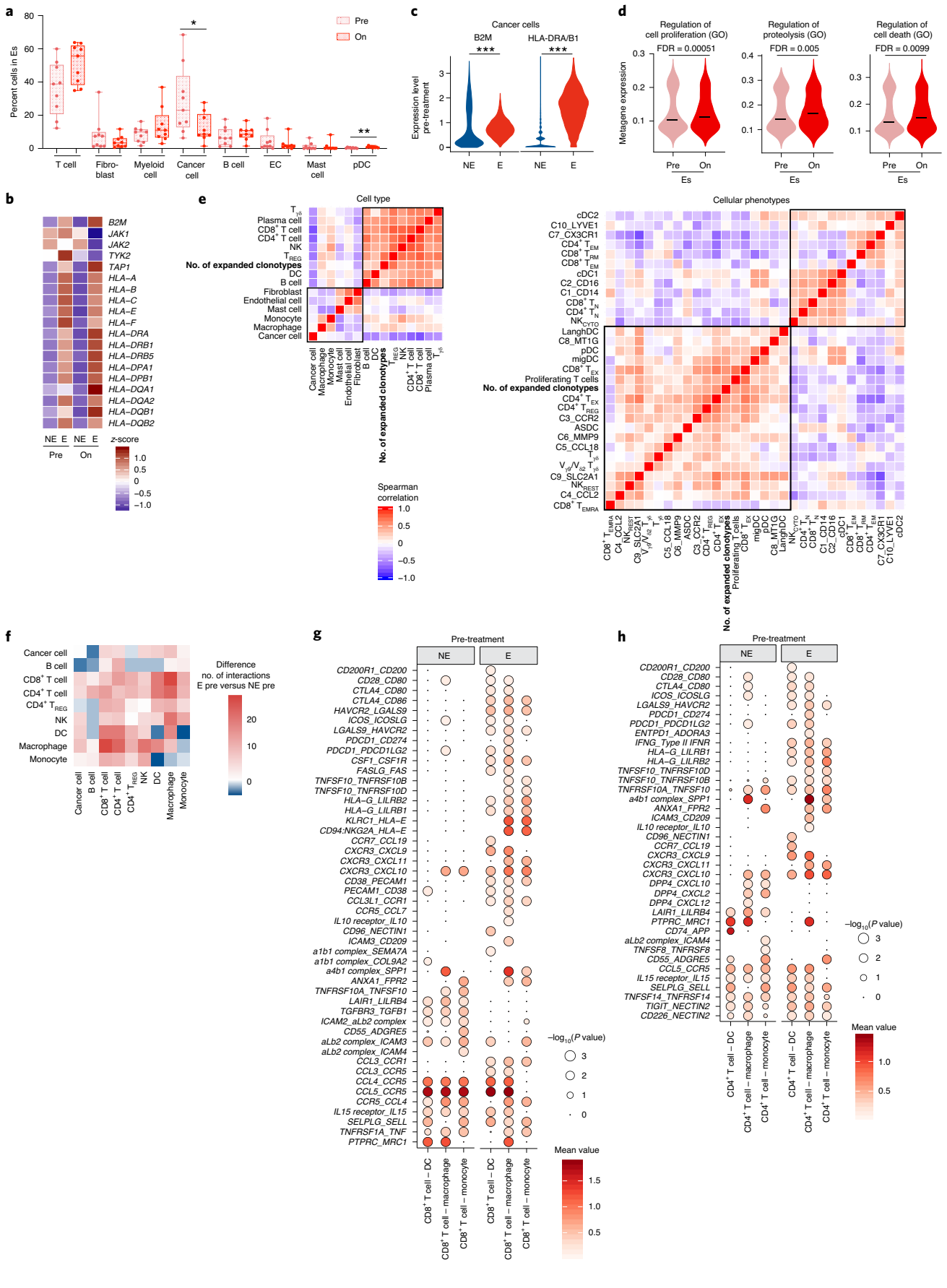
a
Percent cells in Es
Pre
On
T cell
Fibro-blast
Myeloid cell
Cancer cell
B cell
EC
Mast cell
pDC
c
Cancer cells
B2M
HLA-DRA/B1
Expression level pre-treatment
NE
E
d
Regulation of cell proliferation (GO)
FDR = 0.00051
Regulation of proteolysis (GO)
FDR = 0.005
Regulation of cell death (GO)
FDR = 0.0099
Metagene expression
Es
b
B2M
JAK1
JAK2
TYK2
TAP1
HLA–A
HLA–B
HLA–C
HLA–E
HLA–F
HLA–DRA
HLA–DRB1
HLA–DRB5
HLA–DPA1
HLA–DPB1
HLA–DQA1
HLA–DQA2
HLA–DQB1
HLA–DQB2
NE E NE E
Pre On
z-score
e
Cell type
No. of expanded clonotypes
Spearman correlation
Cellular phenotypes
f
Cancer cell
B cell
CD8+ T cell
CD4+ T cell
CD4+ TREG
NK
DC
Macrophage
Monocyte
Difference no. of interactions E pre versus NE pre
g
Pre-treatment
NE
E
CD8+ T cell – DC
CD8+ T cell – macrophage
CD8+ T cell – monocyte
–log10(P value)
Mean value
h
Pre-treatment
CD4+ T cell – DC
CD4+ T cell – macrophage
CD4+ T cell – monocyte
–log10(P value)
Mean value

Fig. 6 | An interactive immune environment positively correlated with T cell expansion. a, Relative percentage of cell types pre- versus on-treatment in Es ($n=9$). Exact P values by two-sided Wilcoxon matched-pairs signed rank test are shown: $^{*}P<0.05$, $^{**}P<0.01$. Boxes show median ± interquartile range; whiskers indicate minima and maxima. **b**, Heatmap showing the expression of genes involved in antigen presentation in cancer cells, comparing Es and NEs, both pre- and on-treatment. **c**, Violin plots showing the differential expression of the indicated proteins by CITE-seq. $^{***}P<0.001$ by two-sided Wilcoxon rank sum test and Bonferroni-corrected (Seurat). **d**, Violin plots showing the metagene expression of the indicated Gene Ontology (GO) signatures in Es both pre- and on-treatment. Horizontal stripes indicate median values. Also shown are false discovery rate (FDR) values by GSEA (hypeR enrichment analysis). **e**, Spearman correlation analysis with the number of expanded T cell clonotypes and the relative abundance of cell types (left) or cellular phenotypes (right) pre-treatment. In each heatmap, two clusters positively or negatively correlating with T cell expansion were identified, as indicated by the outlined boxes. **f**, Difference in the number of significant CellPhoneDB interactions pre-treatment comparing Es and NEs. **g**,**h**, Dotplots showing the significance ($-\log_{10} P$ value) and strength (mean value) of specific interactions pre-treatment between CD8$^+$ (**g**) or CD4$^+$ (**h**) T cells and myeloid cells (DCs, macrophages or monocytes) by comparing Es and NEs.

number of cancer cells decreased on-treatment in Es, this suggests that BC T cell expansion might also be associated with clinical benefit in BC. We additionally observed that the majority of expanding T cell clonotypes were already detected pre-treatment. By contrast, Yost et al. found that in melanoma, expanded clonotypes were not detectable pre-treatment[14]. A difference between both studies is that we profiled on-treatment biopsies ~9 days after starting anti-PD1 treatment, whereas in the study by Yost et al. clonotypes were assessed ~9 weeks after start of treatment. This suggests that pre-existing clonotypes expand immediately after anti-PD1, while several weeks later novel clonotypes start to arise, possibly representing immune responses against secondary antigens arising due to ongoing cell death (a process referred to as antigen spread[41]).

Using trajectory inference, we observed that CD8$^+$ T_{EX} cells expanded along a specific trajectory in Es, exhibiting increased activation and cytotoxic effector function. Interestingly, CD4$^+$ T_{EX} cells, which could be separated into T_{H1} and T_{FH} cells, also contributed to clonal expansion and are likely to also contribute to ICB response. Indeed, studies in mice show that CD4$^+$ T_{H1} cells can enhance CD8$^+$ T cell infiltration[42], while T_{FH} cells drive germinal center formation and subsequent B cell maturation in tertiary lymphoid structures, which can influence the response to ICB[43–45]. Overall, these data illustrate that trajectories are powerful in studying gene expression changes during treatment. It should be stressed, however, that cells originally derived from a tissue but now residing elsewhere will be missed, while unrelated cells infiltrating the tissue will become part of the trajectory. Trajectories should therefore not be interpreted as actual differentiation lineages.

In metastatic BC, PD-L1 positivity in stromal cells predicts benefit from atezolizumab combined with chemotherapy[4], while amplification of the *PD-L1* locus in tumors also associates with therapeutic benefit[5]. We also observed that PD-L1 was associated with T cell expansion, albeit only modestly. By contrast, TILs could not reliably predict T cell expansion, whereas *PD1* and the relative abundance of CD8$^+$ or CD4$^+$ T_{EX} cells emerged as highly predictive markers for T cell expansion. Gene signatures of immune-checkpoint markers or CD4$^+$ T cell activation were also highly predictive, both when anti-PD1 was given to treatment-naive BC or following neoadjuvant chemotherapy. Interestingly, expression of these markers was more pronounced in TNBC than in ER$^+$ BC, possibly explaining why ICB has so far provided the most therapeutic benefit in TNBC.

Our data also suggest molecular targets whose modulation could be synergistic with anti-PD1. For example, we observed how *RUNX3*, which is required for T cell cytotoxicity[46], was downregulated in CD4$^+$ and CD8$^+$ T_{EX} cells of NEs. Hence, reactivation of this pathway could sensitize tumors to anti-PD1. Similarly, we observed potential suppressive interactions with T cells from NEs (for example, LAIR1-LILRB4). Numerous genes were also upregulated along CD8$^+$ T_{EX} and CD4$^+$ T_{H1} trajectories. Several of these (for example, *INPP5F* or *ZEB2*) have not previously been associated with ICB and could represent potential immunoregulatory targets. Finally, increased frequencies of PD-L1-expressing macrophage populations (for example, *CCR2*$^+$ or *MMP9*$^+$ macrophages) or of T cell inhibitory CX3CR1$^+$ macrophages[47,48] were observed, respectively, in Es or NEs. Interestingly, CX3CR1$^+$ macrophages are ablated during ICB in a sarcoma tumor model[49], while genetic ablation of CX3CL1, the ligand of CX3CR1, also inhibited tumor growth and shifted tumor-associated macrophages towards an anti-tumor M1 phenotype[50]. C7_CX3CR1 macrophages also expressed complement *C3*, which suppresses the infiltration and function of CD8$^+$ and CD4$^+$ T cells[51,52]. Overall, this suggests that inhibition of both CX3CR1 or C3 might be therapeutically beneficial.

In conclusion, we present a map of the pre-treatment immune environment that is associated with T cell expansion after neoadjuvant anti-PD1 in patients with BC. This resource could provide insights into potential predictive biomarkers of clinical benefit post-ICB. Follow-up studies involving multiple cycles of anti-PD1 combined with chemotherapy are needed, however, to confirm associations between these biomarkers and clinical responses and to further explore therapeutic targeting of candidate proteins for synergistic use with anti-PD1.

Online content

Any methods, additional references, Nature Research reporting summaries, source data, extended data, supplementary information, acknowledgements, peer review information; details of author contributions and competing interests; and statements of data and code availability are available at https://doi.org/10.1038/s41591-021-01323-8.

Received: 5 June 2020; Accepted: 17 March 2021;
Published online: 6 May 2021

References

1. The Cancer Genome Atlas Network. Comprehensive molecular portraits of human breast tumours. *Nature* **490**, 61–70 (2012).
2. Loi, S. et al. Prognostic and predictive value of tumor-infiltrating lymphocytes in a phase III randomized adjuvant breast cancer trial in node-positive breast cancer comparing the addition of docetaxel to doxorubicin with doxorubicin-based chemotherapy: BIG 02-98. *J. Clin. Oncol.* **31**, 860–867 (2013).
3. Denkert, C. et al. Tumour-infiltrating lymphocytes and prognosis in different subtypes of breast cancer: a pooled analysis of 3,771 patients treated with neoadjuvant therapy. *Lancet Oncol.* **19**, 40–50 (2018).
4. Schmid, P. et al. Atezolizumab plus nab-paclitaxel as first-line treatment for unresectable, locally advanced or metastatic triple-negative breast cancer (IMpassion130): updated efficacy results from a randomised, double-blind, placebo-controlled, phase 3 trial. *Lancet Oncol.* **21**, 44–59 (2020).
5. Bachelot, T. et al. Durvalumab compared to maintenance chemotherapy in metastatic breast cancer: the randomized phase II SAFIR02-BREAST IMMUNO trial. *Nat. Med.* **27**, 250–255 (2021).
6. Schmid, P. et al. Pembrolizumab for early triple-negative breast cancer. *New Engl. J. Med.* **382**, 810–821 (2020).
7. Schmid, P. et al. Pembrolizumab plus chemotherapy as neoadjuvant treatment of high-risk, early-stage triple-negative breast cancer: results from the phase 1b open-label, multicohort KEYNOTE-173 study. *Ann. Oncol.* **31**, 569–581 (2020).
8. Loibl, S. et al. A randomised phase II study investigating durvalumab in addition to an anthracycline taxane-based neoadjuvant therapy in early

triple-negative breast cancer: clinical results and biomarker analysis of GeparNuevo study. *Ann. Oncol.* **30**, 1279–1288 (2019).
9. Chen, D. S. & Mellman, I. Elements of cancer immunity and the cancer-immune set point. *Nature* **541**, 321–330 (2017).
10. Amaria, R. N. et al. Neoadjuvant immune checkpoint blockade in high-risk resectable melanoma. *Nat. Med.* **24**, 1649–1654 (2018).
11. Tumeh, P. C. et al. PD-1 blockade induces responses by inhibiting adaptive immune resistance. *Nature* **515**, 568–571 (2014).
12. Forde, P. M. et al. Neoadjuvant PD-1 blockade in resectable lung cancer. *New Engl. J. Med.* **378**, 1976–1986 (2018).
13. Sade-Feldman, M. et al. Defining T cell states associated with response to checkpoint immunotherapy in melanoma. *Cell* **175**, 998–1013 (2018).
14. Yost, K. E. et al. Clonal replacement of tumor-specific T cells following PD-1 blockade. *Nat. Med.* **25**, 1251–1259 (2019).
15. Lambrechts, D. et al. Phenotype molding of stromal cells in the lung tumor microenvironment. *Nat. Med.* **24**, 1277–1289 (2018).
16. Qian, J. et al. A pan-cancer blueprint of the heterogeneous tumor microenvironment revealed by single-cell profiling. *Cell Res.* **30**, 745–762 (2020).
17. Wauters, E. et al. Discriminating mild from critical COVID-19 by innate and adaptive immune single-cell profiling of bronchoalveolar lavages. *Cell Res.* **31**, 272–290 (2021).
18. Street, K. et al. Slingshot: cell lineage and pseudotime inference for single-cell transcriptomics. *BMC Genomics* **19**, 477 (2018).
19. Zhang, L. et al. Lineage tracking reveals dynamic relationships of T cells in colorectal cancer. *Nature* **564**, 268–272 (2018).
20. Lorenzo-Herrero, S., Sordo-Bahamonde, C., Gonzalez, S. & Lopez-Soto, A. CD107a degranulation assay to evaluate immune cell antitumor activity. *Methods Mol. Biol.* **1884**, 119–130 (2019).
21. Li, H. et al. Dysfunctional CD8 T cells form a proliferative, dynamically regulated compartment within human melanoma. *Cell* **176**, 775–789 e718 (2019).
22. Duhen, T. et al. Co-expression of CD39 and CD103 identifies tumor-reactive CD8 T cells in human solid tumors. *Nat. Commun.* **9**, 2724 (2018).
23. Fu, C. & Jiang, A. Dendritic cells and CD8 T cell immunity in tumor microenvironment. *Front. Immunol.* **9**, 3059 (2018).
24. Villani, A. C. et al. Single-cell RNA-seq reveals new types of human blood dendritic cells, monocytes and progenitors. *Science* **356**, eaah4573 (2017).
25. Collin, M. & Bigley, V. Human dendritic cell subsets: an update. *Immunology* **154**, 3–20 (2018).
26. Maier, B. et al. A conserved dendritic-cell regulatory program limits antitumour immunity. *Nature* **580**, 257–262 (2020).
27. Jackson, S. H., Yu, C. R., Mahdi, R. M., Ebong, S. & Egwuagu, C. E. Dendritic cell maturation requires STAT1 and is under feedback regulation by suppressors of cytokine signaling. *J. Immunol.* **172**, 2307–2315 (2004).
28. Lau, C. M. et al. Transcription factor Etv6 regulates functional differentiation of cross-presenting classical dendritic cells. *J. Exp. Med.* **215**, 2265–2278 (2018).
29. Jiang, W. et al. The receptor DEC-205 expressed by dendritic cells and thymic epithelial cells is involved in antigen processing. *Nature* **375**, 151–155 (1995).
30. Lopez-Albaitero, A. et al. Maturation pathways of dendritic cells determine TAP1 and TAP2 levels and cross-presenting function. *J. Immunother.* **32**, 465–473 (2009).
31. Chow, M. T. et al. Intratumoral activity of the CXCR3 chemokine system is required for the efficacy of anti-PD-1 therapy. *Immunity* **50**, 1498–1512 (2019).
32. Subramanian Vignesh, K. & Deepe, G. S.Jr Metallothioneins: emerging modulators in immunity and infection. *Int. J. Mol. Sci.* **18**, 2197 (2017).
33. Efremova, M., Vento-Tormo, M., Teichmann, S. A. & Vento-Tormo, R. CellPhoneDB: inferring cell-cell communication from combined expression of multi-subunit ligand-receptor complexes. *Nat. Protoc.* **15**, 1484–1506 (2020).
34. Deng, M. et al. LILRB4 signalling in leukaemia cells mediates T cell suppression and tumour infiltration. *Nature* **562**, 605–609 (2018).
35. Thomas, D. A. & Massague, J. TGF-β directly targets cytotoxic T cell functions during tumor evasion of immune surveillance. *Cancer Cell* **8**, 369–380 (2005).
36. Wagner, J. et al. A single-cell atlas of the tumor and immune ecosystem of human breast cancer. *Cell* **177**, 1330–1345 (2019).
37. Jackson, H. W. et al. The single-cell pathology landscape of breast cancer. *Nature* **578**, 615–620 (2020).
38. Savas, P. et al. Single-cell profiling of breast cancer T cells reveals a tissue-resident memory subset associated with improved prognosis. *Nat. Med.* **24**, 986–993 (2018).
39. Fairfax, B. P. et al. Peripheral $CD8^+$ T cell characteristics associated with durable responses to immune checkpoint blockade in patients with metastatic melanoma. *Nat. Med.* **26**, 193–199 (2020).
40. Valpione, S. et al. Immune-awakening revealed by peripheral T cell dynamics after one cycle of immunotherapy. *Nat. Cancer* **1**, 210–221 (2020).
41. Gulley, J. L. et al. Role of antigen spread and distinctive characteristics of immunotherapy in cancer treatment. *J. Natl Cancer Inst.* **109**, djw261 (2017).
42. Nakanishi, Y., Lu, B., Gerard, C. & Iwasaki, A. $CD8^+$ T lymphocyte mobilization to virus-infected tissue requires $CD4^+$ T cell help. *Nature* **462**, 510–513 (2009).
43. Petitprez, F. et al. B cells are associated with survival and immunotherapy response in sarcoma. *Nature* **577**, 556–560 (2020).
44. Helmink, B. A. et al. B cells and tertiary lymphoid structures promote immunotherapy response. *Nature* **577**, 549–555 (2020).
45. Cabrita, R. et al. Tertiary lymphoid structures improve immunotherapy and survival in melanoma. *Nature* **577**, 561–565 (2020).
46. Shan, Q. et al. The transcription factor Runx3 guards cytotoxic $CD8^+$ effector T cells against deviation towards follicular helper T cell lineage. *Nat. Immunol.* **18**, 931–939 (2017).
47. Hart, K. M., Bak, S. P., Alonso, A. & Berwin, B. Phenotypic and functional delineation of murine CX(3)CR1 monocyte-derived cells in ovarian cancer. *Neoplasia* **11**, 564–573 (2009).
48. Zheng, J. et al. Chemokine receptor CX3CR1 contributes to macrophage survival in tumor metastasis. *Mol. Cancer* **12**, 141 (2013).
49. Gubin, M. M. et al. High-dimensional analysis delineates myeloid and lymphoid compartment remodeling during successful immune-checkpoint cancer therapy. *Cell* **175**, 1014–1030 (2018).
50. Korbecki, J. et al. Fractalkine/CX3CL1 in neoplastic processes. *Int. J. Mol. Sci.* **21**, 3723 (2020).
51. Zha, H. et al. Intracellular activation of complement C3 Leads to PD-L1 antibody treatment resistance by modulating tumor-associated macrophages. *Cancer Immunol. Res.* **7**, 193–207 (2019).
52. Kwak, J. W. et al. Complement activation via a C3a receptor pathway alters $CD4^+$ T lymphocytes and mediates lung cancer progression. *Cancer Res.* **78**, 143–156 (2018).

Methods

Patient population and clinical study. The protocol of this single-center, open-label, non-randomized phase 0 study (BioKey) was approved by the local medical ethics committee of the University Hospitals Leuven (S60100) and is provided as a Supplementary Protocol. The primary goal of the study was to evaluate whether one dose of pembrolizumab was able to alter biomarkers related to intratumoral immunity and proliferation in early breast cancer. The study was conducted according to EU legislation regarding ethical regulations and was registered online (NCT03197389). All 54 patients provided written informed consent. We only included patients with a non-metastatic operable newly diagnosed primary invasive carcinoma of the breast that was histologically confirmed as ER$^-$/PR$^-$ or ER$^+$ BC with a primary tumor size of >1 cm, measured by any clinical examination, including mammography, ultrasound or magnetic resonance imaging (detailed clinical information for each patient is provided in Supplementary Tables 1 and 2). The study consisted of two cohorts. The first cohort involved 39 patients scheduled for upfront surgery. Patients had either TNBC, HER2$^+$ (ER$^-$/PR$^-$) or ER$^+$/PR$^\pm$ (HER2$^\pm$) BC. The second cohort consisted of 15 patients who received neoadjuvant chemotherapy and who had clear signs of residual tumor on imaging after three months of neoadjuvant chemotherapy (that is, estimated residual tumor size of at least 10 mm). Patients either had TNBC, ER$^-$/PR$^-$/HER2$^+$ tumors or ER$^+$/PR$^\pm$/HER2$^\pm$ tumors. Chemotherapy was combined with anti-HER2 therapy if the tumor was HER2$^+$. In both cohorts, a single dose of 200 mg pembrolizumab (Keytruda or anti-PD1) was delivered before surgery in a window-of-opportunity setting. Fresh tumor tissue was collected from these patients before (by needle biopsy) and 7–15 (9 ± 2) days after (by resection) pembrolizumab.

Overall, we analyzed 29 patients from the first cohort (treatment-naive early BC) and 11 patients from the second cohort (BC treated with neoadjuvant chemotherapy) by scRNA-seq and scTCR-seq. We did not include 14 patients for the following reasons: two patients were excluded because immediately after study inclusion they refused to have a biopsy taken pre-treatment. Another two patients were not included because we processed tumor tissues with the 3′-scRNA-seq kit from 10x Genomics, which is not compatible with scTCR-seq. We thus could not classify these patients as Es or NEs. For another 10 patients, we failed to obtain high-quality paired biopsies for either the first or second biopsy due to technical limitations of the scRNA-seq technology. Specifically, this was because (1) an insufficient number of cells were obtained after tissue dissociation ($n = 2$), (2) after quality filtering of the scRNA-seq data, <100 cells were retained ($n = 4$), (3) there was limited to no overlap in barcodes between scRNA-seq and scTCR-seq data ($n = 3$) or (4) the on-treatment biopsy contained an unexpected increase in fibroblasts (that is, 50% versus 4% in the pre-treatment biopsy), suggesting that the resection biopsy was taken in the scar tissue of the first biopsy or in a necrotic area. Of these ten patients, seven were treatment-naive prior to receiving anti-PD1 (cohort 1), while three patients received prior chemotherapy (cohort 2).

TIL scoring and immunohistochemistry. Stromal tumor-infiltrating lymphocytes (sTILs) were evaluated according to the guidelines[53] of the International Immuno-oncology Biomarkers Working Group on hematoxylin and eosin (H&E) stained slides. Immunohistochemical stains were performed on 5-µm-thick sections using an automated immunostainer (Bond Max Autostainer, Leica) according to the manufacturer's instructions. A monoclonal antibody was used for Ki67 (clone MIB-1, Agilent) and estrogen receptor (ESR1; MA5-14501, Thermo Fisher) staining. The proliferation marker Ki67 was scored semi-quantitatively by evaluating the nuclear expression of MIB-1 in tumor cells. For ER status, we calculated the Allred score, which is based on the estimated proportion of positively stained tumor cells (0, none; 1, <1%; 2, 1–10%; 3, 11–33%; 4, 34–66%; 5, >66%) combined with an intensity score, which represents the average intensity of positive tumor cells (0, none; 1, weak, 2, intermediate; 3, strong). PD-L1 (Merck 22C3 antibody) immunohistochemistry was performed by Qualtek Molecular Laboratories as per an agreement with Merck. QualTek provided a modified proportion score indicating the proportion of PD-L1-expressing tumor cells and mononuclear inflammatory cells within tumor nests[54,55].

Sample collection and processing. Biopsies were obtained via diagnostic needle biopsy with either a 14-G or 18-G needle (pre-treatment) or surgical resection (on-treatment) and were immediately subjected to single-cell dissociation on ice. From each patient at least two cylinders were collected; one was fixed in formalin and embedded in paraffin for standard histopathology assessment and the other was processed for scRNA-seq. Briefly, the tissue samples were first mechanically dissociated using a scalpel, then enzymatically dissociated in digestion medium (2 mg ml^{-1} Collagenase P (Sigma Aldrich) and 0.2 mg ml^{-1} DNAse I (Roche) in DMEM (Thermo Fisher Scientific)). Red blood cells were removed from the cell suspension using red blood cell lysis buffer (Roche), and the cells were filtered using a 40-µm Flowmi tip strainer (VWR). The number of living cells was determined using a LUNA automated cell counter (Logos Biosystems).

Single-cell RNA-sequencing and T cell repertoire profiling. We performed single-cell TCR-seq and 5′ gene expression profiling on the same single-cell suspension using the Chromium Single Cell V(D)J Solution from 10x Genomics according to the manufacturer's instructions. Up to 5,000 cells were loaded onto a 10x Genomics cartridge for each sample. Cell-barcoded 5′ gene expression libraries were sequenced on an Illumina NextSeq and/or NovaSeq6000 system, and mapped to the GRCh38 human reference genome using CellRanger (10x Genomics). V(D)J enriched libraries were sequenced on an Illumina HiSeq4000 system and TCR alignment and annotation were achieved with CellRanger VDJ (10x Genomics).

Single-cell gene expression analysis. Raw gene expression matrices were generated using CellRanger (10x Genomics) and analyzed using the Seurat[56,57] v3 R package. All cells expressing <200 or >6,000 genes were removed, as well as cells that contained <400 unique molecular identifiers (UMIs) and >15% mitochondrial counts. Samples were merged and normalized. On average, we detected 1,721 genes per cell and 6,021 unique transcripts per cell after filtering. Because every cell has a unique barcode, scRNA-seq data could be linked with the scTCR-seq data.

scRNA-seq clustering leading to cell types. The default parameters of Seurat were used, unless mentioned otherwise. Briefly, for the clustering of all cell types, 2,000 variable genes were identified and principal component analysis (PCA) was applied to the dataset to reduce dimensionality after regressing for the number of UMIs (counts), percentage mitochondrial genes and cell cycle (S and G2M scores were calculated by the *CellCycleScoring* function in Seurat). The 20 most informative principal components (PCs) were used for clustering and Uniform Manifold Approximation and Projection for dimension reduction (UMAP)[58,59]. Clusters in the resulting two-dimensional UMAP representation consisted of distinct cell types, which were identified based on the expression of marker genes. DEGs that functionally characterized the clusters were defined by the MAST test implemented in the *FindAllMarkers* function from Seurat.

scRNA-seq clustering leading to cell subtypes. To subcluster T cells from pre- and on-treatment samples, we used the integration pipeline of Seurat. We regressed for the following confounding factors: number of UMIs (counts), percentage of mitochondrial genes, individual patient, cell cycle and interferon response score (calculated by the *AddModuleScore* function in Seurat using the gene set BROWNE_INTERFERON_RESPONSIVE_GENES from the Molecular Signatures Database or MSigDB v6.2). Regressing for cell cycle and IFN response scores was needed, because failure to regress for them revealed a proliferative and IFN-high cluster, which consisted of multiple heterogeneous T cell phenotypes (Supplementary Fig. 1a–g). When regressing for both variables, we did not identify an IFN-driven subcluster, but still identified a proliferative cluster, which was less heterogeneous with respect to T cell subclusters, and all T cells homogeneously expressed high *PD1* levels. For myeloid cells, a specific clustering approach was used: first, myeloid cell subclustering identified cDC subclusters based on marker gene expression (cCDs: *CLEC9A*, *XCR1*, *CD1C*, *CCR7*, *CCL17*, *CCL19*; Langerhans-like: *CD1A*, *CD207*), as previously described[16]. These DC clusters were excluded from subsequent subclustering efforts, and instead were merged with pDCs for subclustering of DCs, using a similar approach as for T cells with the exception that regression for the IFN response was not needed. All phenotypes were shared between patients, pre- versus on-treatment, and between BC subtypes (Supplementary Fig. 2a–c).

In the second cohort of BC patients receiving neoadjuvant chemotherapy followed by one dose of pembrolizumab, the same clustering approach was used. However, to subcluster T cells, we used the label transfer pipeline from Seurat. Briefly, the annotation of T cells performed in the first cohort served as a reference dataset to assign T cells from the queried data to a given T cell phenotype.

Single-cell copy number analysis. Copy number instability was assessed with the R package inferCNV (https://github.com/broadinstitute/inferCNV; v1.2.1), which is designed to infer copy number alterations from tumor single-cell RNA-seq data. This package compares the expression intensities of genes across malignant cells and relates this to expression in normal cells. A random subset of T cells, B cells and myeloid cells was used as reference, while sex chromosomes were excluded.

Tumor mutation detection and copy number instability. Tumor mutation burden was assessed by whole-exome sequencing as described previously[60]. Briefly, raw reads were mapped with BWA (v0.5.9) to the human reference genome, duplicate reads were removed, and base recalibration and variant calling were performed using GATK 4 (v4.0.5.1) following best practice. Raw variants were considered when present with an allelic frequency of over 10% and when detected in >2 reads. Somatic variants were identified by removing SNPs present in the gnomAD database available on Annovar (version 2017Jul16). The average WES sequencing depth was 102 ± 58× and 85 ± 7% of the exome was covered over 10×. Copy number instability was assessed by low-coverage sequencing as described previously[60]. Briefly, raw sequencing reads were aligned to the human reference genome and duplicates were removed. On average, we obtained 10,145,027 ± 2,150,566 mapped reads. Next, the mapped reads were counted in bins of 50 kb using QDNASeq (v1.14.0) and segmented by ASCAT (v2.5.2). Breakpoints, which we defined as a difference in copy number of at least 0.3 within a chromosome arm, and copy number instability, which we defined as the percentage of the genome with a copy number of <1.7 or >2.3, were calculated in R version 3.6.

Trajectory inference analyses. The R package Slingshot[18] (v1.4) was used to define computationally imputed pseudotime trajectories in T cells. The analyses were performed for $CD8^+$ and $CD4^+$ T cells separately, with $CD4^+$ T_{REG} cells excluded from $CD4^+$ T cells due to their unique developmental origin. For each analysis, PCA-based dimension reduction was performed on DEGs of each phenotype, followed by two-dimensional visualization on UMAP. Graph-based clustering (Louvain) identified additional heterogeneity for some phenotypes; that is, $CD4^+$ T_{EM} cells were split into three subclusters (EM1–3) and T_N cells into two subclusters (N1–2). Next, this UMAP matrix was fed into Slingshot, considering naive T cells as a root state when calculating the trajectories and the pseudotime. These results were used to calculate DEGs between trajectories using TradeSeq (v1.4). We further adapted the TradeSeq concept to identify DEGs for Es versus NEs within the same trajectory by using the *patternTest* function (applying $P < 1 \times 10^{-4}$ and a fold change of >1.5 as threshold), and we clustered genes with similar expression patterns using the *clusterExpressionPatterns* function. For RNA velocity analysis, the spliced and unspliced reads were counted using the velocyto.py package (v0.17.17) from aligned bam files generated by CellRanger[61], and fed into the scVelo package (v0.2.2) to calculate RNA velocity values for each gene of each cell. The resulting RNA velocity vector was embedded into the UMAP space[62].

Differential expression and pathway analysis. DEGs were identified using the MAST test with *FindMarkers* and *FindAllMarkers* functions in Seurat without a threshold for logFC and for expression in a minimum fraction of cells. To identify differentially expressed gene sets, the R package GSVA (Gene Set Variation Analysis) was used to calculate gene set scores per cell and subsequently the R package limma v3.42.1 (linear modeling) to find significantly enriched gene sets. For this analysis, the hallmark (referred to as 'H') and GO ('C5') gene sets were used from the MSigDB v6.2 and were exported using the R package GSEABase (v1.48.0). The R package hypeR (v1.2.0 and v1.5.0) and GO, hallmark and REACTOME gene sets were used for GSEA on DEGs. Only significant genes (adjusted $P < 0.05$) and genes with an avg_logFC higher than log(1.5) or lower than −log(1.5) were used.

Gene signatures. To generate a 50-gene signature for $CD4^+$ T cells, a DEG analysis between $CD4^+$ T cells of Es and NEs was performed, as described above. A Mann–Whitney test (*wilcox.test* in R) was performed to compare the mean expression of all $CD4^+$ T cells per patient between Es ($n = 9$) and NEs ($n = 20$). All genes upregulated in Es with $P < 0.05$ were selected, and the overlap with genes upregulated according to the MAST test (using adjusted $P < 0.05$) was taken. Immunoglobulin, ribosomal and mitochondrial genes were deleted and the 50 genes with the highest fold change were selected for the signature. The $CD4^+$ T_{H1}-activity signature was derived from Zhang et al.[19] by selecting genes upregulated with a ≥2.5 logFC in T_{H1}-like T cells. The HALLMARK_INTERFERON_GAMMA_RESPONSE gene set from MSigDB v6.2 was used for the IFN-γ response signature. Genes included in the cytotoxicity signature are *PRF1*, *GZMB*, *GZMA*, *IFNG*, *NKG7* and *GNLY*. Genes included in the immune checkpoints signature are *CTLA4*, *PDCD1*, *HAVCR2*, *ENTPD1*, *TIGIT*, *LAG3* and *BTLA*. For correlation and ROC analyses we calculated module scores for signatures/pathways using the Seurat function *AddModuleScore* per cell and then averaged per patient pre- or on-treatment. For genes, the average was calculated per patient pre- or on-treatment in the indicated cell (sub)types. Metagenes represent the average of genes in a gene set calculated per cell. We used the pROC (v1.16.2) package in R (default parameters) to generate ROC curves and calculate the associated AUC values[63].

Assessing the TCR repertoire using V(D)J analysis. We obtained 51,499 T cells with a TCR sequence, of which 38,824 cells (75.4%) had paired full-length α and β chains sequenced. We only considered productive TCRs, meaning that they could be joined in the proper reading frame by V(D)J recombination without premature stop codons, enabling expression of a complete TCR α or β chain for downstream analysis. Up to 41,978 of the 46,830 (89.6%) T cells annotated by scRNA-seq (excluding NK cells and γδ T cells) could be linked to a TCR sequence (Supplementary Dataset 11). None of these TCR sequences were shared between patients. TCR clonotypes were defined as TCRs with the same complementarity-determining region 3 (CDR3) nucleotide sequences. A threshold of >2 or >5 cells with the same TCR sequence was used to define clonal cells. We retrieved 1,897 TCR sequences that were present in >2 cells, resulting in 12,531 clonal T cells. When considering a threshold of >5 cells to define a clonal T cell, we detected 568 clonotypes and 7,793 clonal T cells. Clonality was defined as the complement of evenness (that is, 1 – evenness) as previously described by Riaz and colleagues[64], where evenness represents the normalized Shannon entropy. This is the same definition that was referred to as the STARTRAC expansion index in ref. [19].

The evenness value lies between 0 and 1, with a high value indicating a more equal distribution of TCRs and a low value indicating TCR skewing due to clonal expansion. Clonality, which reflects the dominance of particular clones across the TCR repertoire, was calculated per sample. At T cell subtype level, the STARTRAC (https://github.com/Japrin/STARTRAC; v0.1.0) R package was used to calculate STARTRAC expansion or T cell clonality. TCR richness[65], defined as the number of unique TCRs divided by the total number of cells with a unique TCR, was calculated to assess clonotype diversity. The Gini coefficient (or Gini index) was calculated using the ineq (v0.2–13) package in R and was assessed as an alternate measure to calculate the equality of the T cell clonotype distribution. This value ranges between 0 and 1, and the closer it is to 1 the less equal the distribution of clonotypes is[66]. To visualize the degree of TCR clonotypes shared between T cell phenotypes, the connection weight for each pair of T cell phenotypes was calculated as the shared number of unique TCRs divided by the total number of unique TCRs in the T cell phenotype being located first on the trajectory. The resulting network of relatively shared TCRs was plotted using the igraph package (v1.2.5).

Clonotype expansion and contraction. By considering the TCR sequences of T cell clonotypes pre- and on-treatment, we considered a clonotype undergoing expansion when (1) there was an increase in frequency (that is, the number of cells with the same TCR) or proportion (that is, frequency normalized for the number of cells in a sample with a TCR detected) on- versus pre-treatment and (2) a frequency on-treatment of >2. The number of expanded clonotypes upon treatment defined by these two criteria was calculated per patient and had to be >30 to define clonotype expansion. An additional more stringent criterion was applied requiring a clonotype to (1) increase in frequency on- versus pre-treatment and (2) have a frequency on-treatment >5. A threshold of 10 expanded clonotypes defined by this criterion identified patients with clonotype expansion. Clonotypes not detected pre-treatment, but clonal on-treatment (frequency >2 or >5) were also considered as expanded clonotypes. For DEG and pathway analyses, an increase in proportion on- versus pre-treatment as well as a frequency on-treatment of >2 was used to define expanding T cells. Clonotype contraction was defined as the number of TCRs that were clonal pre-treatment, but not on-treatment. Specifically, we considered a clonotype to undergo contraction during treatment when (1) there was a decrease in proportion on- versus pre-treatment, (2) the frequency pre-treatment was >2 and (3) the frequency on-treatment was <2.

Bulk TCR mapping. Bulk TCR-sequencing was performed on RNA extracted from the same resection specimen that was used for scRNA-seq. Reverse-transcription reagents from the single-cell immune profiling kit (10x Genomics) were used for complementary DNA (cDNA) synthesis. cDNA originating from all input RNA was used, rather than from a limited amount of cells. The cDNA was enriched using the chromium Single Cell V(D)J Enrichment kit, Human T Cell (10x Genomics). Enriched libraries were sequenced on an Illumina NovaSeq6000 system. To identify and quantify TCR clonotypes by their β chain, fastq files were analyzed with MiXCR[67,68] (https://github.com/milaboratory/mixcr; v3.0.13). Clonotypes were assembled based on the CDR3 sequence (default). The non-default option to filter out out-of-frame and stop codons (–only-productive) was used. Clonality and richness scores determined by bulk TCR-seq correlated with those obtained by scTCR-seq, confirming that their estimation by scTCR-seq is correct (Supplementary Fig. 3a).

Cell-to-cell communication of scRNA-seq data. The CellPhoneDB algorithm (https://github.com/Teichlab/cellphonedb; v2.1.1) was used to infer cell-to-cell interactions. Briefly, the algorithm allows the detection of ligand–receptor interactions between cell types in scRNA-seq data using the statistical framework described in refs. [69,33]. We took the union of the significant interactions found in NEs pre-treatment, NEs on-treatment, Es pre-treatment and Es on-treatment to explore specific interactions. Next, we assessed the amount of interactions that are shared and specific for (1) pre-treatment Es versus NEs and (2) pre- versus on-treatment Es, and explored specific interactions indicated as curated (that is, annotated by the CellPhoneDB developers) (Supplementary Dataset 10).

CITE-seq. We used the CITE-seq protocol described by Stoeckius et al.[70] with small modifications. Up to 100,000–500,000 single cells of breast tumors were suspended in 100 µl of staining buffer (2% BSA/0.01% Tween in PBS) before addition of 10 µl of Fc blocking reagent (FcX, BioLegend) and subsequent 10-min incubation on ice. This was followed by the addition of 25 µl of TotalSeq A (Biolegend) 198 antibody-oligo pool (1:1,000 diluted in staining buffer; Supplementary Dataset 12) and another 30-min incubation on ice with mild vortex every 10 min. Cells were washed three times with staining buffer and filtered through a 40-µm Flowmi strainer before loading with 10x Genomics 3′ scRNA-seq library kits into a 10x Genomics Chromium controller. ADT (antibody-derived tag) additive primers (1 µl from 1 M stock) were added for cDNA polymerase chain reaction (cDNA PCR) to increase the yield of ADT products. ADT-derived and mRNA-derived cDNAs were separated by solid-phase reversible immobilization purification and amplified separately for library construction and subsequent sequencing by a HiSeq4000 or NovaSeq6000 system. Raw sequencing reads were demultiplexed and feature counts matrices were created with CellRanger. These matrices were further processed with Seurat. Cells with >400 features were retained. Overall, CITE-seq was successful on eight patients, of which two were Es, resulting in CITE-seq data on 33,119 cells. Data were processed after center-log ratio normalization. To identify the cell identity of these retained cells, we iteratively clustered with PCA dimensional reduction and *t*-distributed stochastic neighbor embedding visualization and annotated the cell types based on established markers. Clustering based on protein data revealed the major cell types T, B, myeloid, cancer, endothelial and mast cells,

as well as fibroblasts (Supplementary Fig. 3b,c). We failed to identify DCs because few DC-specific antibodies were included in the panel. CITE-seq annotated 94.0% of cells to the same cell type as scRNA-seq. Moreover, we were able to further distinguish $CD4^+$, $CD8^+$ and regulatory T cells as well as NK cells ($n = 8{,}338$; Supplementary Fig. 3d,e). To assess the differences between E and NE patients or pre- versus on-treatment, the Wilcoxon rank sum test was used and P values were Bonferonni-corrected for multiple testing.

Reporting Summary. Further information on research design is available in the Nature Research Reporting Summary linked to this Article.

Data availability

Raw sequencing reads of all single-cell experiments (scRNA-seq, scTCR-seq and CITE-seq) have been deposited in the European Genome-phenome Archive (EGA) under study no. EGAS00001004809 (with a summary of the BioKey study and patient characteristics) and with data accession no. EGAD00001006608 (to access the data itself under restricted access). Requests for accessing raw sequencing reads will be reviewed by the UZLeuven-VIB data access committee. Any data shared will be released via a Data Transfer Agreement that will include the necessary conditions to guarantee protection of personal data (according to European GDPR law). Alternately, a download of the read count data per individual patient is publicly available at http://biokey.lambrechtslab.org. The publicly available gnomAD database (https://gnomad.broadinstitute.org) was used to filter tumor exome-seq data for somatic mutations and calculate tumor mutation burden. Raw sequencing reads of all exome and low-coverage whole-genome sequencing experiments are also provided under EGAS00001004809.

References

53. Salgado, R. et al. The evaluation of tumor-infiltrating lymphocytes (TILs) in breast cancer: recommendations by an International TILs Working Group 2014. *Ann. Oncol.* **26**, 259–271 (2015).
54. Emancipator, K. Keytruda and PD-L1: a real-world example of co-development of a drug with a predictive biomarker. *AAPS J.* **23**, 5 (2020).
55. Dolled-Filhart, M. et al. Development of a prototype immunohistochemistry assay to measure programmed death ligand-1 expression in tumor tissue. *Arch. Pathol. Lab. Med.* **140**, 1259–1266 (2016).
56. Stuart, T. et al. Comprehensive integration of single-cell data. *Cell* **177**, 1888–1902 (2019).
57. Butler, A., Hoffman, P., Smibert, P., Papalexi, E. & Satija, R. Integrating single-cell transcriptomic data across different conditions, technologies and species. *Nat. Biotechnol.* **36**, 411–420 (2018).
58. Mclnnes, L., Healy, J. & Melville, J. UMAP: Uniform Manifold Approximation and Projection for dimension reduction. Preprint at https://arxiv.org/pdf/1802.03426.pdf (2018).
59. Becht, E. et al. Dimensionality reduction for visualizing single-cell data using UMAP. *Nat. Biotechnol.* **37**, 38–44 (2019).
60. Boeckx, B. et al. The genomic landscape of nonsmall cell lung carcinoma in never smokers. *Int. J. Cancer* **146**, 3207–3218 (2020).
61. La Manno, G. et al. RNA velocity of single cells. *Nature* **560**, 494–498 (2018).
62. Bergen, V., Lange, M., Peidli, S., Wolf, F. A. & Theis, F. J. Generalizing RNA velocity to transient cell states through dynamical modeling. *Nat. Biotechnol.* **38**, 1408–1414 (2020).
63. Robin, X. et al. pROC: an open-source package for R and S+ to analyze and compare ROC curves. *BMC Bioinformatics* **12**, 77 (2011).
64. Riaz, N. et al. Tumor and microenvironment evolution during immunotherapy with nivolumab. *Cell* **171**, 934–949 (2017).
65. Zhu, W. et al. A high density of tertiary lymphoid structure B cells in lung tumors is associated with increased $CD4^+$ T cell receptor repertoire clonality. *Oncoimmunology* **4**, e1051922 (2015).
66. Thomas, P. G., Handel, A., Doherty, P. C. & La Gruta, N. L. Ecological analysis of antigen-specific CTL repertoires defines the relationship between naive and immune T-cell populations. *Proc. Natl Acad. Sci. USA* **110**, 1839–1844 (2013).
67. Bolotin, D. A. et al. MiXCR: software for comprehensive adaptive immunity profiling. *Nat. Methods* **12**, 380–381 (2015).
68. Bolotin, D. A. et al. Antigen receptor repertoire profiling from RNA-seq data. *Nat. Biotechnol.* **35**, 908–911 (2017).
69. Vento-Tormo, R. et al. Single-cell reconstruction of the early maternal–fetal interface in humans. *Nature* **563**, 347–353 (2018).
70. Stoeckius, M. et al. Simultaneous epitope and transcriptome measurement in single cells. *Nat. Methods* **14**, 865–868 (2017).

Acknowledgements

The BioKey study was supported by an MSD grant to A.S., by Fonds Nadine De Beauffort to A.S., by a 'Kom op Tegen Kanker' to A.S. and H.W., by the Stichting Tegen Kanker and the Flemish Fund for Scientific Research (FWO; project G0B6120N) Belgium, by Agilent Technologies (Thought Leader award) to D.L. This VIB Grand Challenges project also received support from the Flemish Government under Management Agreement 2017–2021 (VR 2016 2312 doc.1521/4), from the European Union's Horizon 2020 Research and Innovation Programme under grant agreement no. 847912 (RESCUER) and from KU Leuven grant (C14/18/092) Symbiosys3. A.D.G. acknowledges financial support from the Research Foundation Flanders (FWO; Fundamental Research grant, G0B4620N; Excellence of Science/EOS grant, 30837538, for 'DECODE' consortium), KU Leuven (C1 grant, C14/19/098; POR award funds, POR/16/040) and Kom op Tegen Kanker/KOTK (KOTK/2018/11509/1). L.V.D. was supported by an aspirant FWO grant. G.F. is recipient of a post-doctoral mandate from the Klinsche Onderzoek en OpleidingsRaad (KOOR) of the University Hospitals Leuven. The computational resources and services used in this work were provided by the VSC (Flemish Supercomputer Center), funded by the Research Foundation—Flanders (FWO) and the Flemish Government (department EWI). None of these funders had a role in study design, data collection and analysis, decision to publish or preparation of the manuscript. We thank T. Van Brussel and R. Schepers for technical assistance.

Author contributions

D.L. and J.Q. designed and supervised the single-cell experiments and wrote the manuscript. A.S. designed the clinical study and supervised sample collection and clinical annotation, with important help from H.V., as well as I.N., K.P., P.N. and H.W. G.F. and K.L. performed and interpreted all histopathological data including TIL scoring. Data analysis was performed by A.B. and J.Q., with substantial contributions from L.v.D., B.B. and M.v.B. C.D., I.A. and A.D.G. contributed critical data interpretation. All authors read or provided comments on the manuscript.

Competing interests

The authors declare no competing interests.

Additional information

Extended data is available for this paper at https://doi.org/10.1038/s41591-021-01323-8.

Supplementary information The online version contains supplementary material available at https://doi.org/10.1038/s41591-021-01323-8.

Correspondence and requests for materials should be addressed to J.Q., A.S. or D.L.

Peer review information *Nature Medicine* thanks Matthew Spitzer, Justin Balko and Aditya Bardia for their contribution to the peer review of this work. Saheli Sadanand was the primary editor on this article and managed its editorial process and peer review in collaboration with the rest of the editorial team.

Reprints and permissions information is available at www.nature.com/reprints.

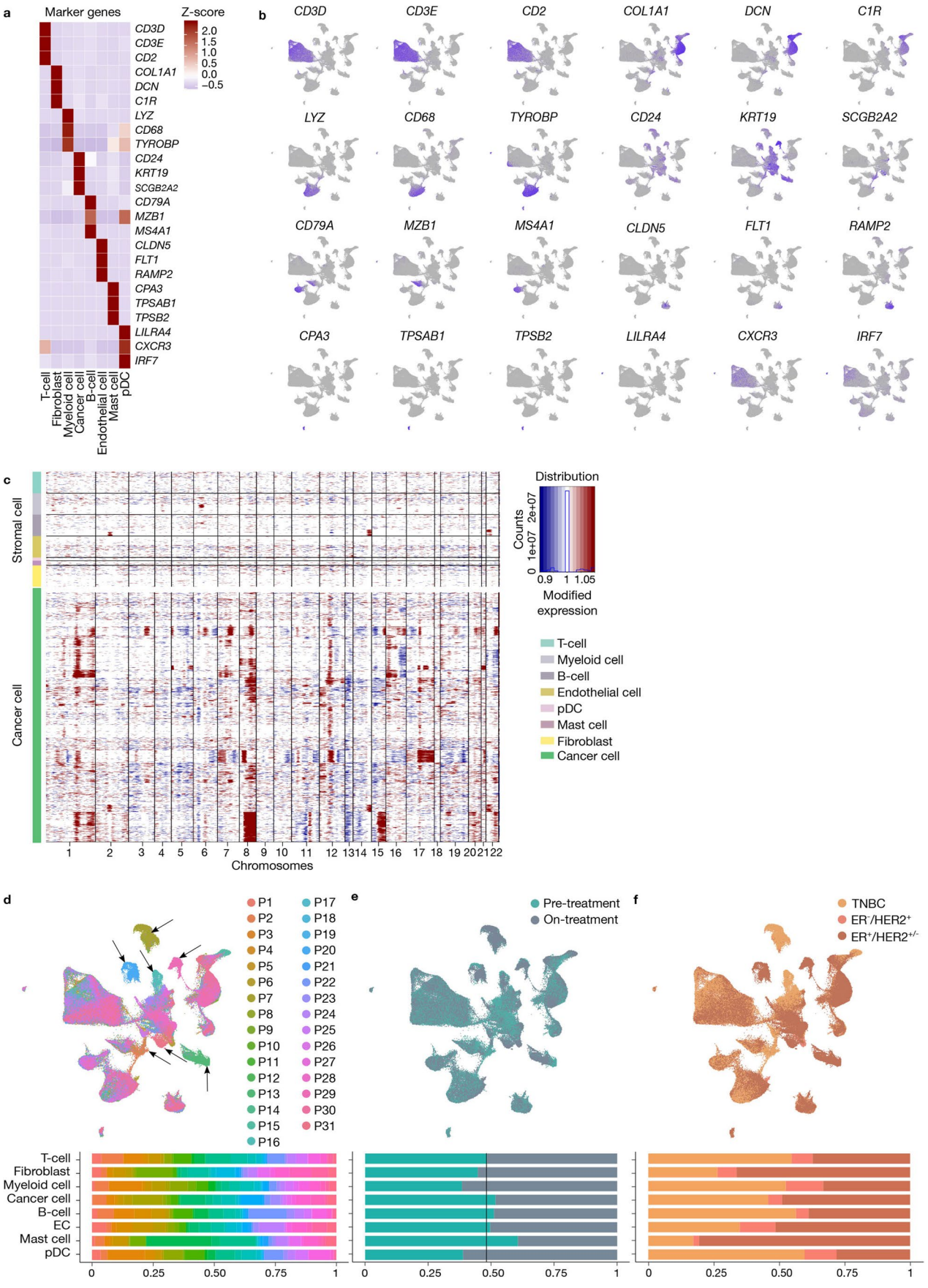

Extended Data Fig. 1 | See next page for caption.

Extended Data Fig. 1 | Cell types detected based on scRNA-seq profiling of 175,942 cells. a,b, Heatmap (**a**) and UMAP (**b**) showing the expression of 3 marker genes for each cell type. **c**, CNV profile in cancer *versus* stromal cells assessed using InferCNV based on scRNA-seq. **d-f**, UMAP and barplots color-coded for individual patients (**d**), pre- *versus* on-treatment biopsies (**e**) and BC subtype (**f**) showing their distribution across cell types. pDC: plasmacytoid dendritic cell; CNV: copy number variation.

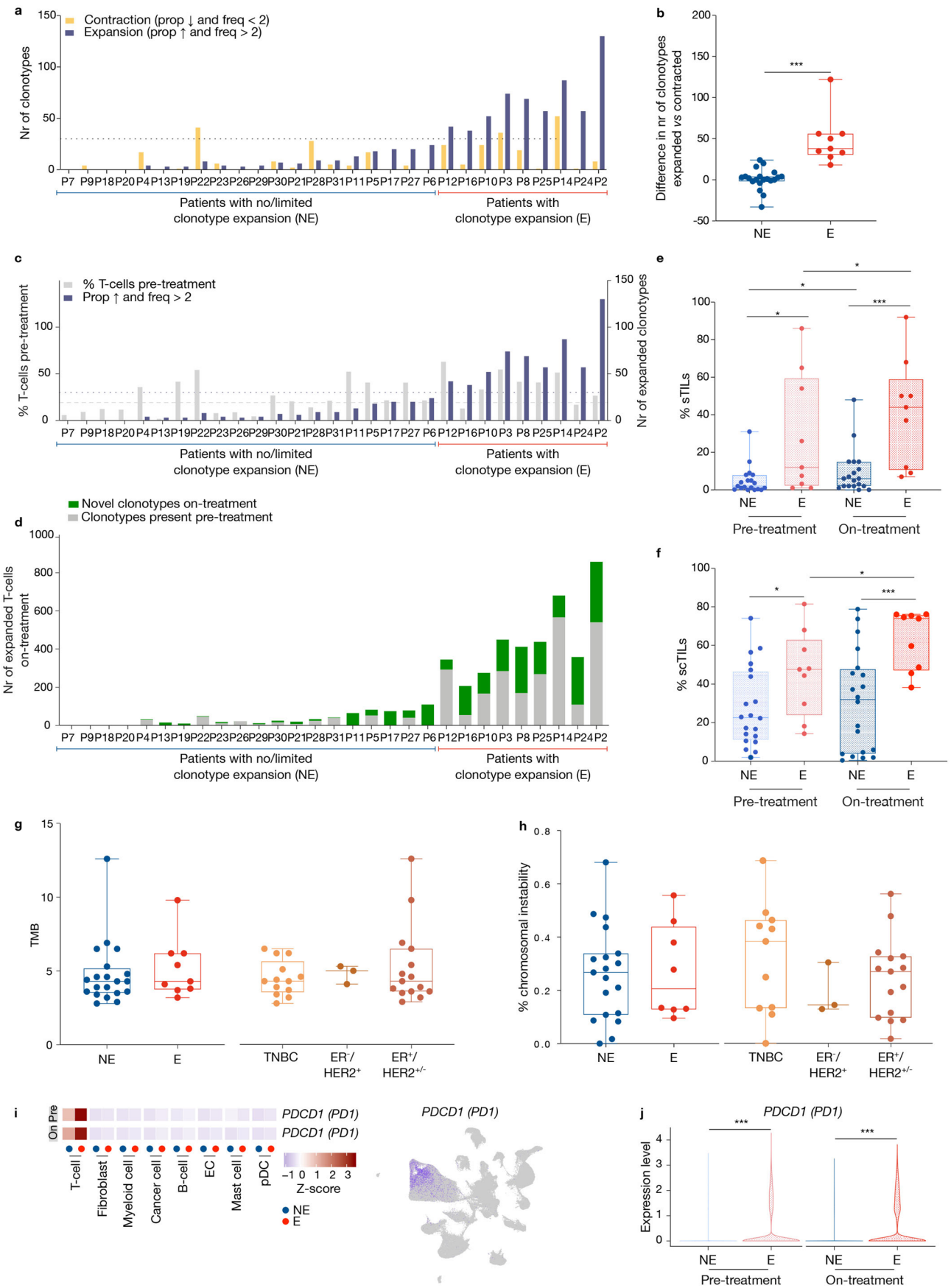

Extended Data Fig. 2 | See next page for caption.

Extended Data Fig. 2 | T-cell expansion *versus* contraction, TIL-scores and *PD1* expression. a, Number of clonotypes that contract (yellow) compared to the number of clonotypes that expand (purple) per patient. A clonotype was considered to undergo T-cell expansion when it increased in proportion on- *versus* pre-treatment and the frequency on-treatment was >2 (purple). A clonotype was considered to undergo T-cell contraction when it decreased in proportion on- *versus* pre-treatment and the frequency on-treatment was < 2 (yellow). **b**, Boxplot showing the difference in number of expanded *versus* contracted clonotypes, comparing Es ($n=9$) *versus* NEs ($n=20$). **c**, Percentage of T-cells in the pre-treatment biopsy (gray) per patient compared to the number of expanded clonotypes after anti-PD1 (proportion data from Fig. 1a are shown). Horizontal dotted lines indicate the thresholds used to define tumors with a high % of T-cells (gray) or with T-cell expansion (purple). **d**, Number of expanding T-cells per patient with clonotypes not present (novel clonotypes; green) or present (pre-existing clonotypes; gray) pre-treatment. Up to 61% (range: 27-85%) of expanded T-cells in Es on-treatment had clonotypes already present pre-treatment. **e**, Percentage of stromal TILs (sTILs) by histopathology on a hematoxylin and eosin stained slide, comparing Es ($n=9$) *versus* NEs ($n=19$). **f**, Percentage of TILs based on scRNA-seq (scTILs) determined by the fraction of B- and T-cells in each sample, comparing Es ($n=9$) *versus* NEs ($n=20$). **g-h**, Tumor mutation burden (TMB) (**g**) and chromosomal instability (**h**) in Es ($n=9$ for TMB, $n=8$ for chromosomal instability) *versus* NEs ($n=20$ for TMB, $n=19$ for chromosomal instability) and for each BC subtype; TNBC ($n=13$ for TMB, $n=11$ for chromosomal instability), $ER^{-}/HER2^{+}$ ($n=3$) and $ER^{+}/HER2^{\pm}$ ($n=15$). **i**, Heatmap of normalized *PD1* and UMAP color-coded for *PD1*. **j**, Normalized *PD1* expression in T-cells. Panels **b**, **e-h**: exact P values by Mann-Whitney test or Wilcoxon matched-pairs signed rank test for paired samples (pre- *versus* on-treatment); two-sided (**b**, **e**, **g-h**) or one-sided (**f**); *P < 0.05, *P < 0.01, ***P < 0.001. Panel **j**: ***P < 0.001 by MAST test and Bonferonni-corrected (Seurat). Panels **b**, **e-h**: box, median ± interquartile range; whiskers, minimum and maximum.

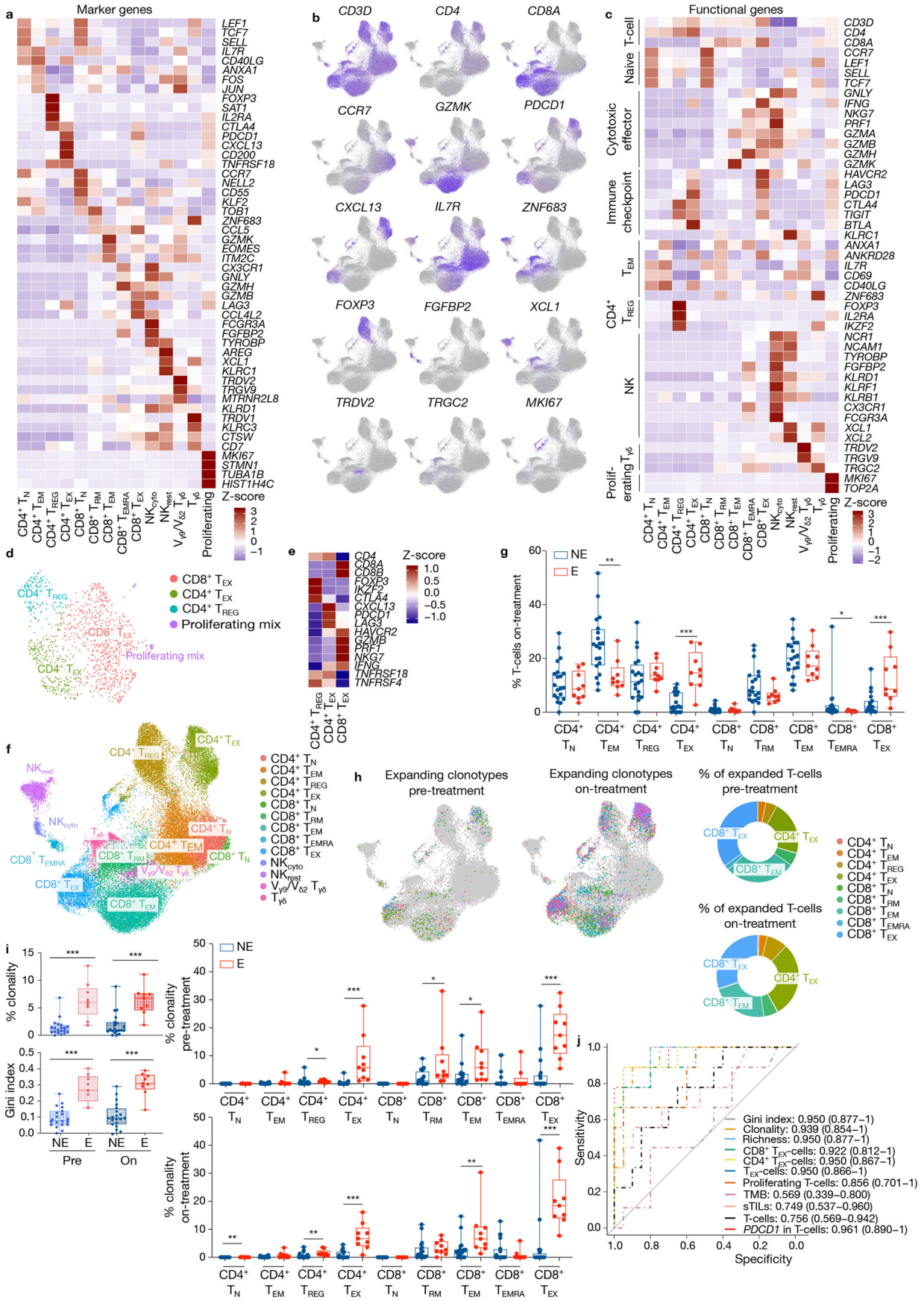

Extended Data Fig. 3 | See next page for caption.

Extended Data Fig. 3 | T-cell phenotypes during anti-PD1 treatment. a, Heatmap showing expression of marker genes for the 14 T-/NK-cell phenotypes. **b**, UMAP color-coded for marker gene expression of T-/NK-cell phenotypes. **c**, Heatmap showing expression of functional genes in the 14 T-/NK-cell phenotypes. **d**, UMAP depicting the T-cell phenotypes detected in the proliferative T-cell subcluster. **e**, Heatmap showing marker gene expression for T_{REG}, $CD4^+$ and $CD8^+$ T_{EX}-cells in the proliferative T-cell subcluster. **f**, T-/NK-cell phenotypes after assigning proliferating T-cells to their respective subtype ($CD4^+$, $CD8^+$ T_{EX}-cells and $CD4^+$ T_{REG}). **g**, Relative contribution (in %) of each T-cell phenotype in on-treatment biopsies, comparing Es ($n = 9$) *versus* NEs ($n = 20$). **h**, UMAP showing all T-cell clonotypes expanding on-treatment (left panel) and pie charts showing the distribution of expanding T-cells across T-cell phenotypes (right panel) in Es. Each clonotype on the UMAP has a specific color and clonotypes in pre- and on-treatment tissues are shown separately. **i**, T-cell clonality, Gini index and T-cell clonality of each T-cell phenotype both pre- (upper panel) and on-treatment (lower panel), comparing Es ($n = 9$) *versus* NEs ($n = 20$). **j**, ROC curves for the indicated parameter pre-treatment to predict T-cell expansion. AUC values and 95% confidence intervals are shown. Panels **g** and **i:** exact P values by two-sided Mann-Whitney test or Wilcoxon matched-pairs signed rank test for paired samples (pre- *versus* on-treatment); $^*P < 0.05$, $^*P < 0.01$, $^{***}P < 0.001$. Panels **g** and **i**: box, median ± interquartile range; whiskers, minimum and maximum.

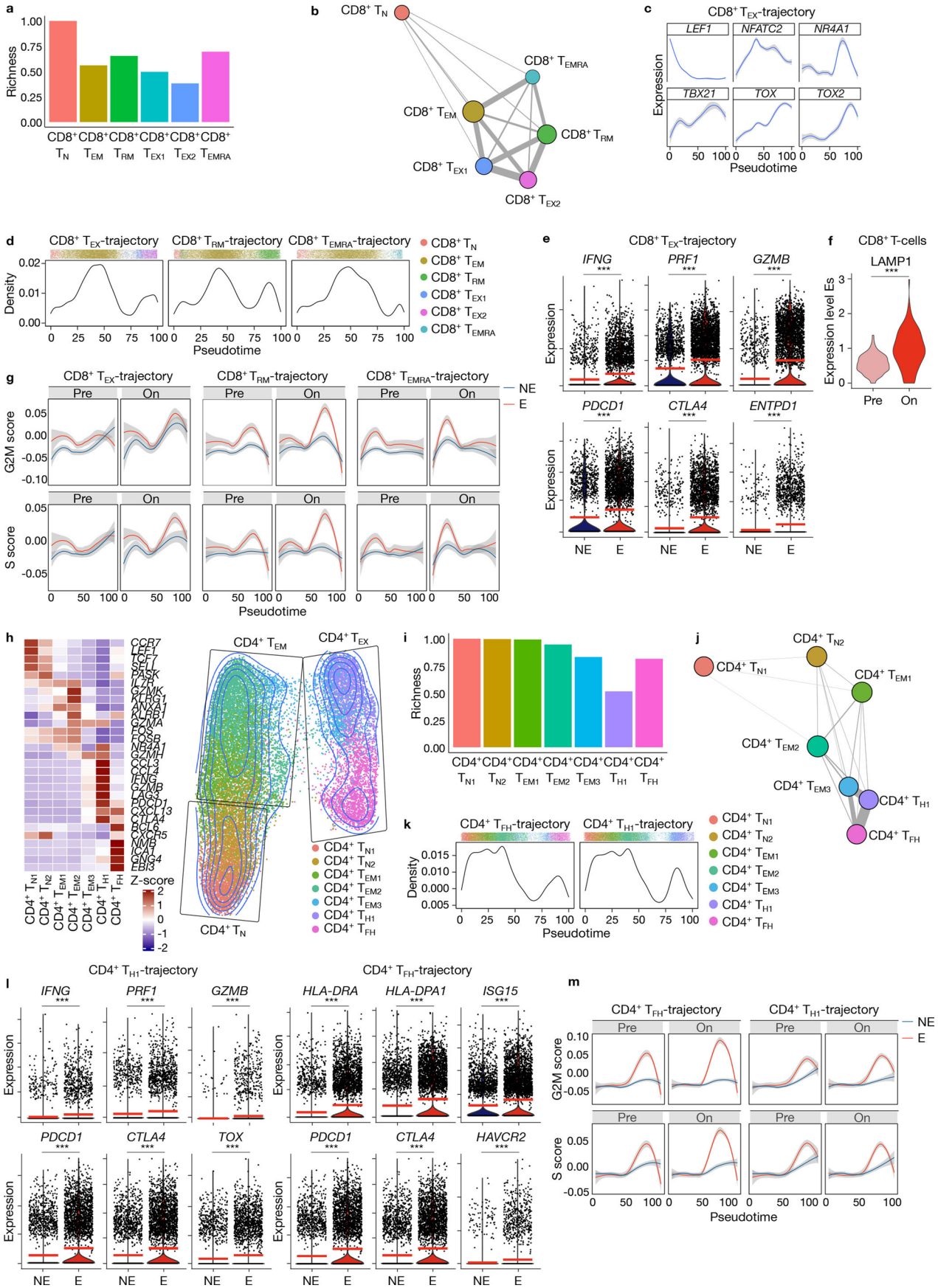

Extended Data Fig. 4 | See next page for caption.

Extended Data Fig. 4 | Analysis of expanding T-cells trajectories. a, Barplots showing TCR richness for the indicated $CD8^+$ T-cell phenotype. **b**, Clonotype sharing (thickness indicates proportion of sharing) between $CD8^+$ T-cell phenotypes. **c**, Expression dynamics of transcription factors (TFs) along the $CD8^+$ T_{EX}-trajectory. **d**, Density plots reflecting the relative number of T-cells combined. **e**, Violin plots showing expression of T-cell effector, cytotoxicity and exhaustion markers in $CD8^+$ T_{EX}-cells on-treatment. ***$P < 0.001$ by two-sided Wilcoxon rank sum test per gene. **f**, LAMP1 expression by CITE-seq. ***$P < 0.001$ by two-sided Wilcoxon rank sum test and Bonferroni-corrected (Seurat). **g**, Cell cycle scores along the $CD8^+$-trajectories pre- and on-treatment in E *versus* NE. **h**, Heatmap (left panel) and 2D density UMAP (right panel) showing that the major $CD4^+$ T-cell phenotypes ($CD4^+$ T_N, T_{EM}, T_{EX}) can be split into subclusters with corresponding marker genes. **i**, Barplots showing TCR richness for the indicated $CD4^+$ T-cell phenotype. **j**, Clonotype sharing (thickness indicates proportion of sharing) between the $CD4^+$ T-cell phenotypes. **k**, Density plots reflecting the relative number of T-cells combined. **l**, Violin plots showing expression of T-cell effector, cytotoxicity and exhaustion markers in $CD4^+$ T_{H1}- and T_{FH}-cells on-treatment. ***$P < 0.001$ by two-sided Wilcoxon rank sum test per gene. **m**, Cell cycle scores along the $CD4^+$-trajectories. Gray shades in panel **c**, **g** and **m** represent the 95% confidence interval at any given pseudotime.

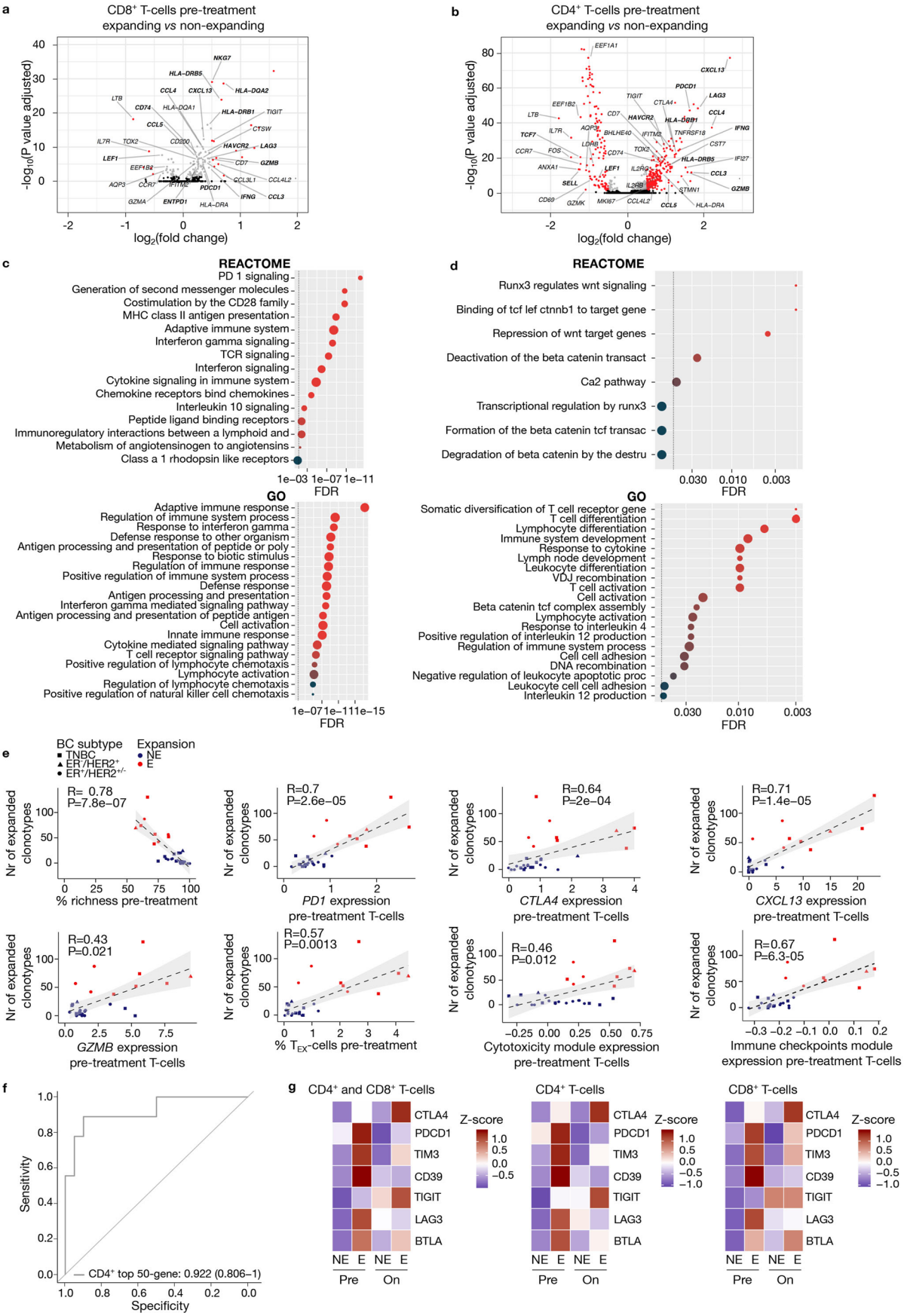

Extended Data Fig. 5 | See next page for caption.

Extended Data Fig. 5 | Expression signatures and phenotypes predictive of T-cell expansion. a,b, Volcano plot showing DEGs between CD8$^+$ (**a**) and CD4$^+$ (**b**) T-cells that expand *versus* those that not expand pre-treatment. Black dots: P=ns; gray: $P < 0.05$; red: $P < 0.05$ and absolute log2FC≥0.5. P values by MAST test and Bonferroni-corrected (Seurat). Genes in bold are discussed in the manuscript. **c-d**, GSEA (hypeR) on genes up- or down-regulated in pre-treatment T-cells that expand (**c**) *versus* T-cells that do not expand upon treatment (**d**) on REACTOME (upper panel) and GO (lower panel) pathways. **e**, Scatterplots showing Spearman correlations between the number of expanded clonotypes *versus* the abundance of phenotypes, or average expression of marker genes and signature module scores per patient. Signature module scores were calculated using the Seurat function *AddModuleScore* per cell and then averaged per patient. P values by two-sided Spearman's rank correlation test. R values are Spearman's rank correlation coefficients (rho). **f**, ROC curve based on the average module expression of our 50-gene signature in CD4$^+$ T-cells (excluding T_{REG}) pre-treatment to predict T-cell expansion. AUC-value and 95% confidence interval are shown. **g**, Heatmap showing protein expression of 7 immune stimulation-induced immune-checkpoints in all T-cells, CD8$^+$ and CD4$^+$ T-cells.

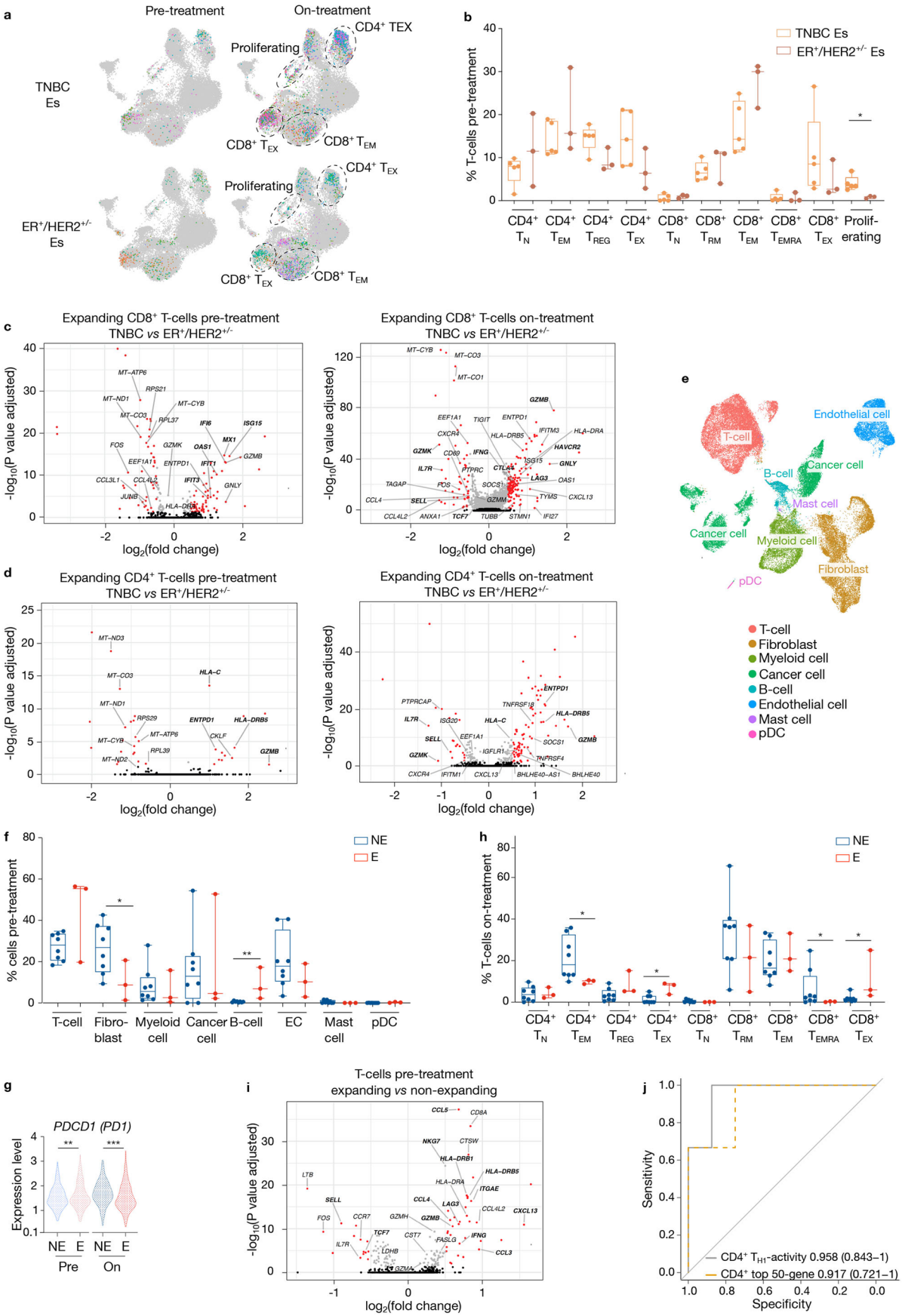

Extended Data Fig. 6 | See next page for caption.

Extended Data Fig. 6 | T-cell expansion according to BC subtype and in patients receiving neoadjuvant chemotherapy followed by anti-PD1. a, UMAP pre- and on-treatment color-coded for expanded clonotypes in TNBC ($n=5$; upper panel) and ER$^+$/HER2$^\pm$ ($n=3$; lower panel) Es. **b**, Relative contribution of T-cells pre-treatment in Es, comparing TNBC ($n=5$) and ER$^+$/HER2$^\pm$ ($n=3$). **c**, Volcano plots showing DEGs for CD8$^+$ expanding T-cells in TNBC *versus* ER$^+$/HER2$^\pm$ Es pre-treatment (left panel) and on-treatment (right panel). **d**, Volcano plots showing DEGs for CD4$^+$ expanding T-cells in TNBC *versus* ER$^+$/HER2$^\pm$ Es pre-treatment (left panel) and on-treatment (right panel). **e**, UMAP of 50,693 cells from $n=11$ BC patients with neoadjuvant chemotherapy followed by anti-PD1 (replication cohort or cohort 2) by scRNA-seq color-coded for the indicated cell type. **f**, Relative contribution of each cell type (in %) pre-treatment in the replication cohort, comparing Es ($n=3$) *versus* NEs ($n=8$). **g**, Normalized *PD1* expression in T-cells (cohort 2). **h**, Relative contribution of each T-cell phenotype (in %) on-treatment in the replication cohort, comparing Es ($n=3$) *versus* NEs ($n=8$). **i**, Volcano plot showing DEGs between pre-treatment T-cells that expand ($n=347$ cells) *versus* those that do not expand ($n=3159$ cells) in the replication cohort. **j**, ROC curve based on the average module expression of T_{H1}-activity and our 50-gene signature in CD4$^+$ T-cells (excluding T_{REG}) pre-treatment to predict T-cell expansion. AUC values and 95% confidence intervals are shown. Black dots in Volcano plots (panels **c**, **d** and **i)**: P=ns; gray: $P<0.05$; red: $P<0.05$ and absolute log2FC≥0.5. P values Volcano plots by MAST test and Bonferroni-corrected (Seurat). Genes in bold are discussed in the manuscript. Panels **b**, **f** and **h**: exact P values by two-sided (**b**) or one-sided (**f**,**h**) Mann-Whitney test; *$P<0.05$, *$P<0.01$, ***$P<0.001$. Panels **b**, **f** and **h**: box, median ± interquartile range; whiskers, minimum and maximum. Panel **g**: **$P<0.01$, ***$P<0.001$ by MAST test (Seurat).

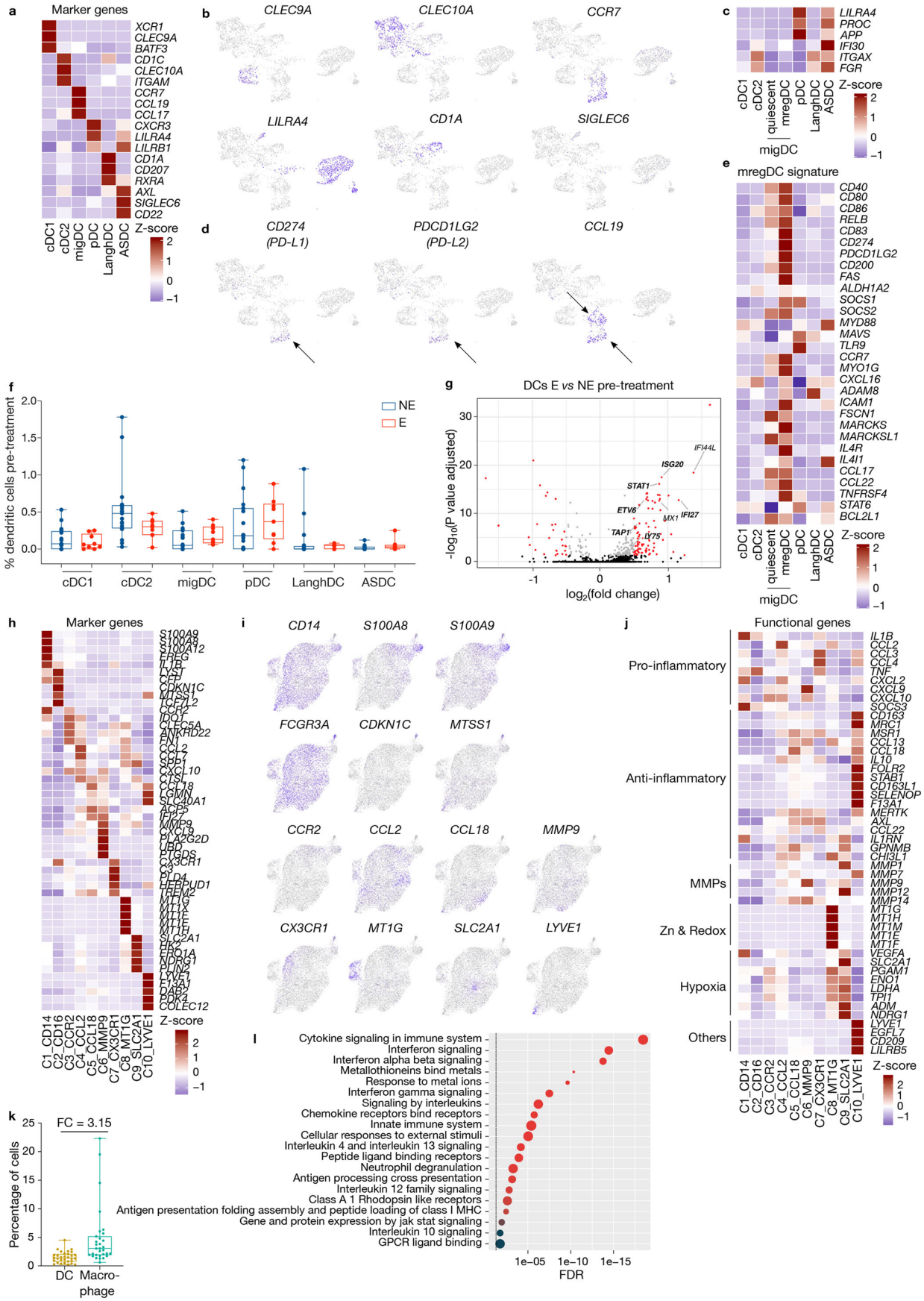

Extended Data Fig. 7 | See next page for caption.

Extended Data Fig. 7 | DC and monocyte/macrophage subclustering. a, Heatmap showing 3 marker genes for each DC phenotype. **b**, UMAP of DCs color-coded for one marker gene per DC phenotype. **c**, Heatmap of genes specific for cDC2 and pDC showing that ASDCs share characteristics of cDC2s and pDCs. **d**, UMAP of DCs color-coded for *PD-L1/L2* and *CCL19*. **e**, Heatmap showing expression of the mregDC signature described by Maier and colleagues[26] across DC phenotypes. **f**, Relative contribution of each DC phenotype (in %) to all cells pre-treatment, comparing Es ($n=9$) *versus* NEs ($n=20$). P>0.05 for all by two-sided Mann-Whitney test. Box, median ± interquartile range; whiskers, minimum and maximum. **g**, Volcano plot showing DEGs in DCs comparing Es *versus* NEs pre-treatment. Black dots: P=ns; gray: $P<0.05$; red: $P<0.05$ and absolute log2FC ≥ 0.5. P values by MAST test and Bonferroni-corrected (Seurat). Genes in bold are discussed in the manuscript. **h**, Heatmap showing marker genes for each myeloid cell phenotype. **i**, UMAP of myeloid cells color-coded for one marker gene per myeloid cell phenotype. **j**, Heatmap showing expression of functional genes in the 10 myeloid cell phenotypes. **k**, Boxplot showing relative percentage of DCs and macrophages detected in each patient ($n=31$) by scRNA-seq. Box, median ± interquartile range; whiskers, minimum and maximum. FC: fold change. **l**, GSEA (hypeR) based on REACTOME for DEGs in macrophages comparing Es *versus* NEs pre-treatment.

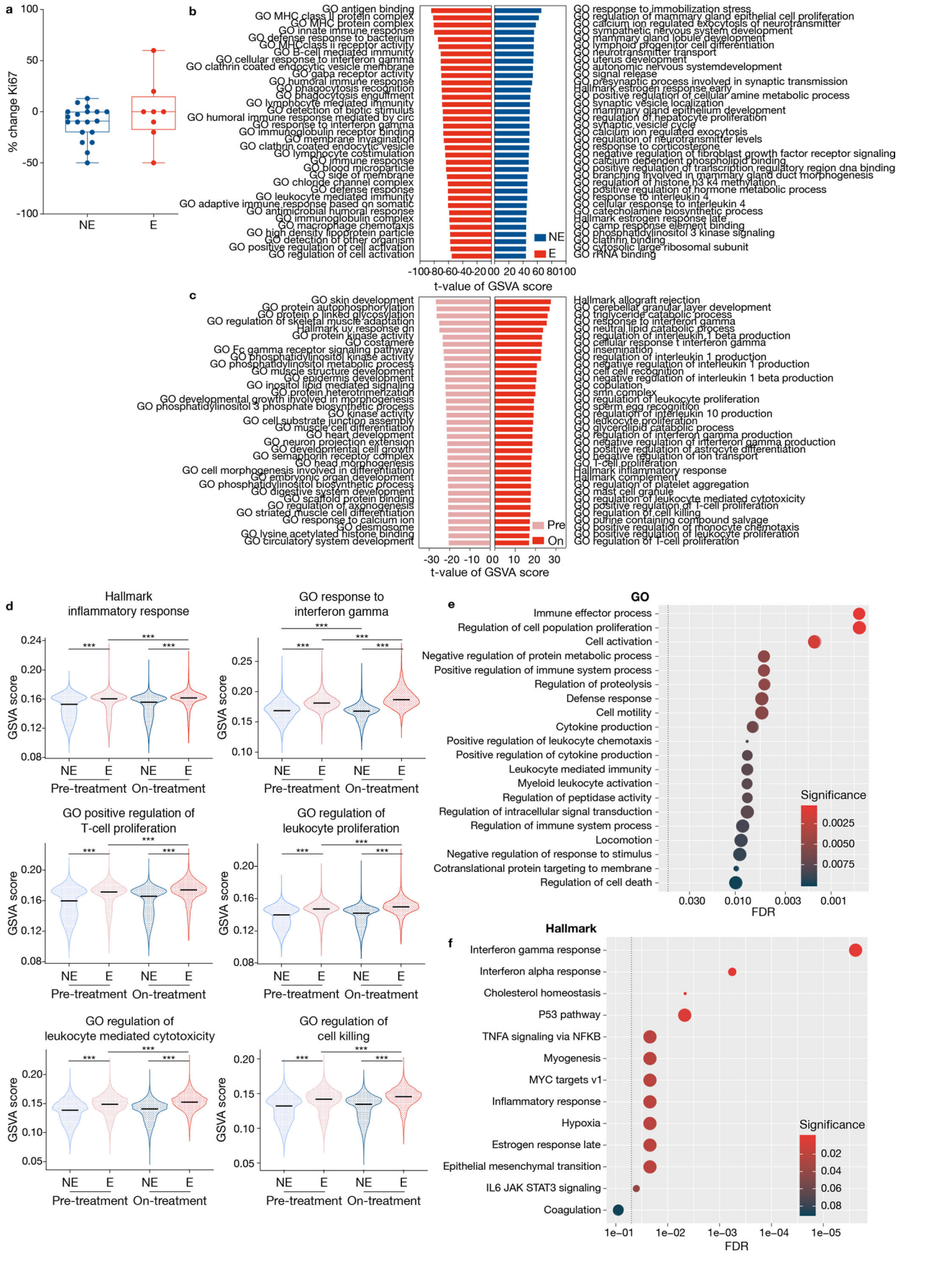

Extended Data Fig. 8 | See next page for caption.

Extended Data Fig. 8 | Pathway analysis in cancer cells. a, Change in Ki67 positivity (by immunohistochemistry) comparing paired on- *versus* pre-treatment biopsies in Es ($n = 8$) *versus* NEs ($n = 19$). Box, median ± interquartile range; whiskers, minimum and maximum. **b-c**, Differences in pathway activities scored per cell by GSVA pre-treatment in Es *versus* NEs (**b**) and on- *versus* pre-treatment in Es (**c**). Shown are the top 35 pathways based on absolute t-values obtained by a linear model. **d**, Violin plots showing GSVA scores for the indicated pathways. Stripes indicate median values. ***$P < 0.001$ (Benjamini-Hochberg adjusted) and absolute t-value>10 by a linear model. **e-f**, GSEA of DEGs upregulated on-treatment in cancer cells of Es using hypeR on GO (**e**) and hallmark gene sets (**f**). Genes driving enrichment included *CD74*, *HLA-DQA1* (antigen presentation), *IDO1* (antigen-dependent T-cell activation), *A2M* (tumour migration and growth), *CXCL10* and *CXCL14* (chemoattractant of immune cells), *CHI3L1* (IFN production).

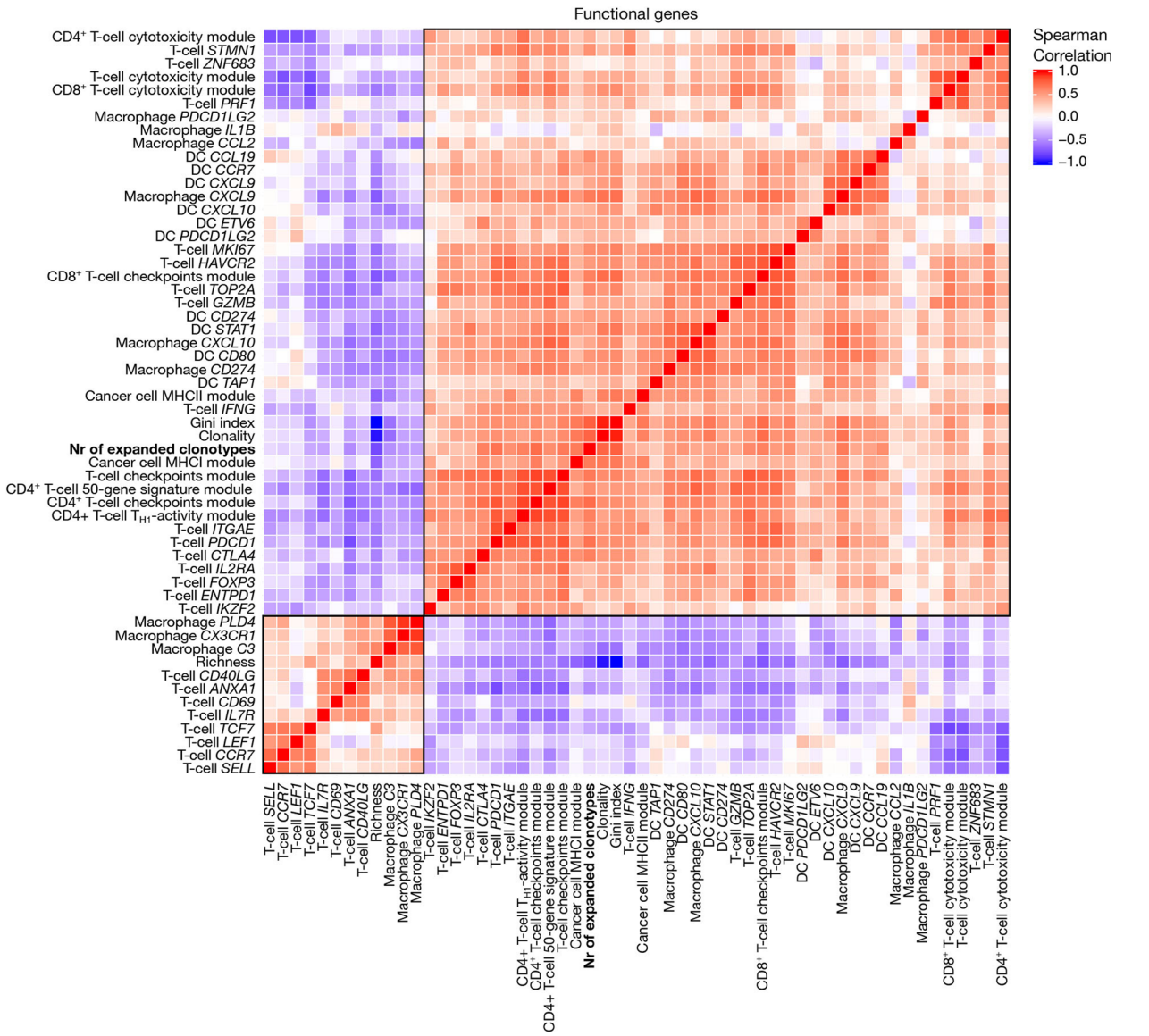

Extended Data Fig. 9 | Immune context analysis. Spearman correlation between the number of expanded clonotypes and other key functional marker genes or signature modules pre-treatment. Average expression of genes was calculated in the indicated (sub)cell type pre-treatment per patient. In each heatmap two clusters positively or negatively correlating with expansion were identified, as indicated by the squared boxes.

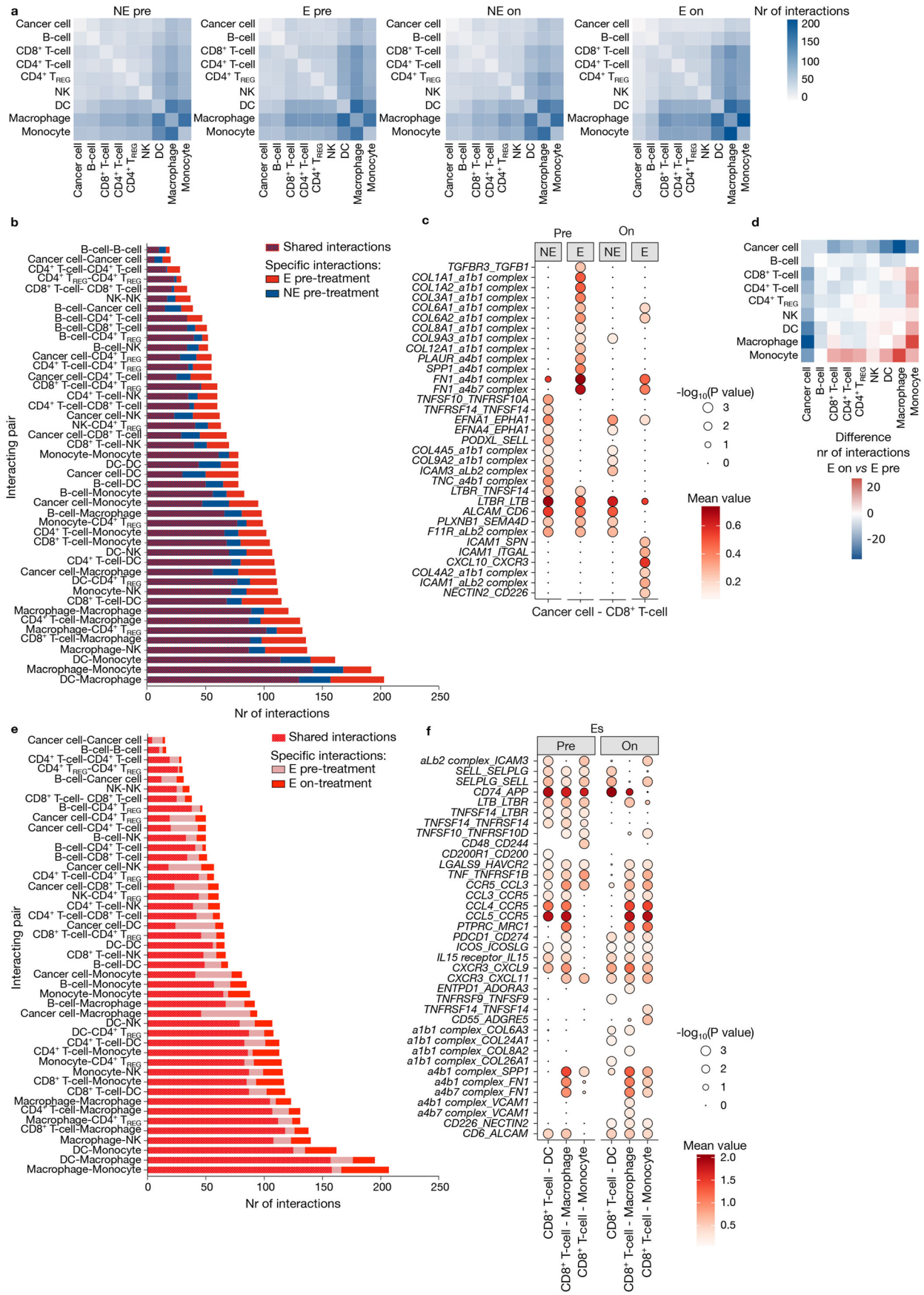

Extended Data Fig. 10 | See next page for caption.

Extended Data Fig. 10 | Cell-to-cell type interactions by CellPhoneDB. a, Heatmap showing the number of interactions in NEs pre-treatment, in Es pre-treatment, NEs on-treatment and Es on-treatment. **b**, Barplot showing for each cell-to-cell type interaction, the number of interactions shared and specific pre-treatment comparing Es *versus* NEs. **c**, Dotplot showing the significance (-$\log_{10}$ P value) and strength (mean value) of specific interactions between cancer cells and $CD8^+$ T-cells comparing Es *versus* NEs. The aLb2 complex refers to ITGAL and ITGB2, which together form LFA-1 **d**, Difference in the number of significant CellPhoneDB interactions in Es comparing pre- *versus* on-treatment. **e**, Barplot showing per cell-to-cell type interactions, the number of interactions shared and specific in pre- *versus* on-treatment biopsies from Es. **f**, Dotplot showing the significance (-$\log_{10}$ P value) and strength (mean value) of specific interactions in Es between $CD8^+$ T-cells and myeloid cells (either DCs, macrophages or monocytes) pre- *versus* on-treatment.

nature research

Corresponding author(s): Diether Lambrechts

Last updated by author(s): 12/03/2021

Reporting Summary

Nature Research wishes to improve the reproducibility of the work that we publish. This form provides structure for consistency and transparency in reporting. For further information on Nature Research policies, see our Editorial Policies and the Editorial Policy Checklist.

Statistics

For all statistical analyses, confirm that the following items are present in the figure legend, table legend, main text, or Methods section.

n/a	Confirmed
☐	☒ The exact sample size (*n*) for each experimental group/condition, given as a discrete number and unit of measurement
☐	☒ A statement on whether measurements were taken from distinct samples or whether the same sample was measured repeatedly
☐	☒ The statistical test(s) used AND whether they are one- or two-sided *Only common tests should be described solely by name; describe more complex techniques in the Methods section.*
☒	☐ A description of all covariates tested
☐	☒ A description of any assumptions or corrections, such as tests of normality and adjustment for multiple comparisons
☐	☒ A full description of the statistical parameters including central tendency (e.g. means) or other basic estimates (e.g. regression coefficient) AND variation (e.g. standard deviation) or associated estimates of uncertainty (e.g. confidence intervals)
☐	☒ For null hypothesis testing, the test statistic (e.g. *F*, *t*, *r*) with confidence intervals, effect sizes, degrees of freedom and *P* value noted *Give P values as exact values whenever suitable.*
☒	☐ For Bayesian analysis, information on the choice of priors and Markov chain Monte Carlo settings
☒	☐ For hierarchical and complex designs, identification of the appropriate level for tests and full reporting of outcomes
☐	☒ Estimates of effect sizes (e.g. Cohen's *d*, Pearson's *r*), indicating how they were calculated

Our web collection on statistics for biologists contains articles on many of the points above.

Software and code

Policy information about availability of computer code

Data collection	Single-cell RNA sequencing reads were mapped to the GRCh38 human reference genome and processed into gene expression matrices with CellRanger (10x Genomics; version 2.1.1, 2.2.0, 3.0.2 and 3.1.0). TCR (V(D)J) alignment and annotation was achieved with CellRanger VDJ (10x Genomics, version 2.1.1, 2.2.0, 3.0.2 and 3.1.0).
Data analysis	Single-cell RNA-sequencing data was analyzed using Seurat (version 3). Single-cell CNV analysis was done using inferCNV (https://github.com/broadinstitute/inferCNV; version 1.2.1). Trajectory inference analysis was done with SlingShot (version 1.4). TradeSeq (version 1.4) was used to calculate differential expressed genes between the trajectories inferred by SlingShot. For the RNA velocity analysis we used CellRanger, the velocyto.py package (version 0.17.17) and the scVelo package (version 0.2.2). To identify and quantify TCR clonotypes by their beta chain, fastq files were analyzed with MiXCR (https://github.com/milaboratory/mixcr; version 3.0.13). The CellPhoneDB algorithm (https://github.com/Teichlab/cellphonedb; version 2.1.1) was used to infer cell-to-cell interactions. GSVA (Gene Set Variation Analysis; version 1.34.0) was used to calculate gene set scores per cell and limma (version 3.42.1) to find significantly enriched gene sets. The hallmark (referred to as 'H') and Gene Ontology (GO; 'C5') gene sets were used from the MSigDB (version 6.2; http://www.gsea-msigdb.org/gsea/msigdb/index.jsp) and were exported using GSEABase (version 1.48.0). ROC analyses were done with the R package pROC (version 1.16.2). The R package hypeR (version 1.2.0 and 1.5.1 for trajectory-related analyses) and GO, hallmark and REACTOME gene sets were used for gene set enrichment analysis on differentially-expressed genes. STARTRAC (https://github.com/Japrin/STARTRAC; version 0.1.0) was used to calculate STARTRAC-expansion (i.e., clonality) at T-cell subtype level. The R package ineq (version 0.2-13) was used to calculate the Gini coefficient or index. To plot networks of relatively shared TCRs the igraph R package (version 1.2.5) was used. For the assessment of tumor mutation burden BWA (version 0.5.9) was used for mapping raw whole-exome sequencing reads and GATK 4 (version 4.0.5.1) for base recalibration and variant calling. Somatic variants were identified by removing SNPs present in the gnomAD database (https://gnomad.broadinstitute.org) available on Annovar (version 2017 July 16th). For the assessment of copy-number instability mapped low-coverage sequencing reads were counted in bins of 50kb using QDNASeq (version 1.14.0) and segmented by ASCAT (version 2.5.2).

For manuscripts utilizing custom algorithms or software that are central to the research but not yet described in published literature, software must be made available to editors and reviewers. We strongly encourage code deposition in a community repository (e.g. GitHub). See the Nature Research guidelines for submitting code & software for further information.

Data

Policy information about availability of data

All manuscripts must include a data availability statement. This statement should provide the following information, where applicable:

- Accession codes, unique identifiers, or web links for publicly available datasets
- A list of figures that have associated raw data
- A description of any restrictions on data availability

Raw sequencing reads of all single-cell experiments (scRNA-seq, scTCR-seq and CITE-seq) have been deposited under restricted access in the European Genome-phenome Archive (EGA) with study submission number EGAS00001004809 and data accession number EGAD00001006608. Requests for raw sequencing reads will be reviewed by the UZLeuven-VIB data access committee. Any data shared will be released via a Data Transfer Agreement that will include the necessary conditions to guarantee protection of personal data (according to the European GDPR law). Alternatively, a download of the read count data per individual patient is publicly available at http://biokey.lambrechtslab.org. The publicly available gnomAD database (https://gnomad.broadinstitute.org) was used to filter tumor exome-seq data for somatic mutations and calculate tumor mutation burden. Raw sequencing reads of the exome-seq experiments are also provided via the EGAS00001004809 study submission number.

Field-specific reporting

Please select the one below that is the best fit for your research. If you are not sure, read the appropriate sections before making your selection.

☒ Life sciences ☐ Behavioural & social sciences ☐ Ecological, evolutionary & environmental sciences

For a reference copy of the document with all sections, see nature.com/documents/nr-reporting-summary-flat.pdf

Life sciences study design

All studies must disclose on these points even when the disclosure is negative.

Sample size	This was a single-center, open-label, non-randomized phase 0 study (BioKey). The primary goal of the study was to evaluate whether one dose of pembrolizumab was able to alter biomarkers related to intratumoral immunity and proliferation in early breast cancer. As this study does not have a clinical response of outcome-related end-point, we did not perform a sample size calculation. Instead, the number of patients included in the study was based on anticipated number of patients diagnosed with early breast cancer in the University Hospital Leuven during a recruitment period of 1 year. The assumptions for the sample size were as follows: >600 patients with early breast cancer are diagnosed and treated at the Leuven Multidisciplinary Breast Center (MBC; University Hospitals Leuven) on a yearly basis. Roughly 20% (120 patients) of these are ER/PR-negative. Of these, 25% (30 patients) is expected to receive upfront surgery and 75% (90 patients) upfront chemotherapy. After upfront chemotherapy 45% of patients is expected to have residual disease (>1cm; 40 patients). In total, 70 patients are therefore expected to be eligible for the suggested prospective study. Participation of 50% of eligible patients would allow inclusion of 34 patients after 1 year. Approximately 66% (400 patients) of all patients treated at the Leuven MBC have ER-positive breast cancer. 10% of these ER-positive patients are expected to be eligible for this trial taking into account the tumour size after neo-adjuvant therapy. Participation of 50% of eligible patients would allow inclusion of 20 patients within 1 year. This brings us to a total of 34 ER/PR-negative and 20 ER-positive patients, or 54 patients in total. We therefore recruited patients until we reached the total of 54 patients. Recruitment was done independent of the number of ER-positive or ER/PR-negative patients, and independently of the number of patients being treatment-naïve or receiving prior chemotherapy at the time of inclusion. Overall, we profiled biopsies from 54 patients.
Data exclusions	Out of 54 patients, we did not include 14 patients for the following reasons: 2 patients were excluded because immediately after study inclusion they refused to have a biopsy taken pre-treatment. Another 2 patients were not included because we processed tumor tissues with the 3'-scRNA-seq kit from 10x Genomics, which is not compatible with scTCR-seq. Therefore, we could not classify these patients as Es or NEs. For another 10 patients, we failed to obtain high-quality paired biopsies for either the 1st or 2nd biopsy due to technical limitations of the scRNA-seq technology. Specifically, this was because (i) an insufficient number of cells was obtained after tissue dissociation (n=2), (ii) after quality filtering of the scRNA-seq data <100 cells were retained (n=4), (iii) there was limited to no overlap in barcodes between scRNA-seq and scTCR-seq data (n=3), (iv) the on-treatment biopsy contained an unexpected increase of fibroblasts (i.e., 50% versus 4% in the pre-treatment biopsy) suggesting the resection biopsy was taken in scar tissue of the first biopsy or in a necrotic area. Out of these 10 patients, 7 patients were treatment-naive prior to receiving anti-PD1 (cohort 1), while 3 patients received prior chemotherapy (cohort 2).
Replication	This is not applicable since no technical replicates were used, only biological replicates. Indeed, due to very high costs of scRNA-seq and the scarcity of tumor tissue obtained by needle biopsy, and due to the fact that it is not ethical to take an unlimited number of needle biopsies from a breast cancer patient, we could not include technical replicates for the single-cell analyses.
Randomization	Patients were not randomized in this study. All patients received standard-of-care treatment, undergoing upfront surgery of their treatment-naïve tumor (n=29 patients in cohort 1) or receiving neo-adjuvant chemotherapy for 20-24 weeks prior to surgery (n=11 patients in cohort 2). According to standard clinical guidelines, patients undergoing immediate surgery have a tumor size >2cm and/or optimal surgery should be feasible, whereas patients receiving systemic chemotherapy have a tumor size <2cm and/or optimal surgery is not feasible. All patients recruited in the study then received in a window-of-opportunity setting 1 dose of pembrolizumab prior to surgery. Since all patients received pembrolizumab, it was not necessary to randomize patients. Where needed, a post-hoc stratification for prior chemotherapy (cohort 1 versus cohort 2) or for BC subtype (ER/PR-negative versus ER-positive disease) was performed in the data analysis phase.
Blinding	There was no blinding in this study, because all patients received standard-of-care treatment followed by one dose of pembrolizumab. This was a phase 0 window-of-opportunity open-label study, in which the sponsor, investigator and patient were always aware of the treatment that was administered. The main purpose of this study was to investigate the effect of a single dose of pembrolizumab on TIL scores across

breast cancer subtypes and to monitor changes in TIL scores. Therefore, since all patients received the pembrolizumab, blinding was not applicable.

Reporting for specific materials, systems and methods

We require information from authors about some types of materials, experimental systems and methods used in many studies. Here, indicate whether each material, system or method listed is relevant to your study. If you are not sure if a list item applies to your research, read the appropriate section before selecting a response.

Materials & experimental systems

n/a	Involved in the study
☐	☒ Antibodies
☒	☐ Eukaryotic cell lines
☒	☐ Palaeontology and archaeology
☒	☐ Animals and other organisms
☐	☒ Human research participants
☐	☒ Clinical data
☒	☐ Dual use research of concern

Methods

n/a	Involved in the study
☒	☐ ChIP-seq
☒	☐ Flow cytometry
☒	☐ MRI-based neuroimaging

Antibodies

Antibodies used

The following antibodies were used for standard immunohistochemistry experiments: Ki67 (clone MIB-1, IR62661-2, Agilent; ready to use), ESR1 (SP1, MA5-14501, ThermoFisher; 1:200 diluted), PD-L1 (Merck 22C3 antibody; immunohistochemistry was performed by Qualtek Molecular Laboratories (Newtown PA, USA) as per agreement with Merck).

We also used 198 oligo-conjugated antibodies (1:1000 diluted in staining buffer) from the TotalSeq™-A panel to perform CITE-seq. The panel is a commercially available and distributed by BioLegend (TotalSeq™-A Human Universal Cocktail, V1.0, Cat #: 399907). The TotalSeq™-A Human Universal Cocktail has been designed to react with unique cell surface antigens of human origin. It contains monoclonal lyophilized antibodies that are provided in optimized concentrations to provide a ready-to-use solution once the cocktail has been reconstituted. The following antibodies (with clone name): CD80 (2D10), CD86 (IT2.2), CD274 (29E.2A3), CD273 (24F.10C12), CD275 (2D3), CD276 (DCN.70), CD11b (M1/70), Galectin-9 (9M1-3), CD270 (122), CD252 (11C3.1), CD137L (5F4), CD155 (SKII.4), CD112 (TX31), CD47 (CC2C6), CD70 (113-16), CD30 (BY88), CD48 (BJ40), CD277 (BT3.1), CD40 (5C3), CD154 (24-31), CD52 (HI186), CD3 (UCHT1), CD8 (SK1), CD45 (2D1), CD19 (HIB19), CD33 (P67.6), CD11c (S-HCL-3), CD34 (581), CD138 (MI15), CD269 (19F2), β2-microglobulin (2M2), HLA-A,B,C (W6/32), CD90 (5E10), CD117 (104D2), CD10 (HI10a), CD45RA (HI100), CD123 (6H6), CD7 (CD7-6B7), CD105 (43A3), CD201 (RCR-401), CD49f (GoH3), CD194 (L291H4), CD4 (RPA-T4), CD44 (IM7), CD15 (MC-480), CD8a (RPA-T8), CD14 (M5E2), CD16 (3G8), CD56 (QA17A16), CD25 (BC96), CD45RO (UCHL1), CD279 (EH12.2H7), TIGIT (A15153G), Mouse IgG1, κ isotype Ctrl (MOPC-21), Mouse IgG2a, κ isotype Ctrl (MOPC-173), Mouse IgG2b, κ isotype Ctrl (MPC-11), Rat IgG2b, κ isotype Ctrl (RTK4530), CD20 (2H7), CD335 (9E2), CD294 (BM16), CD45R/B220 (RA3-6B2), CD326 (9C4), CD31 (WM59), CD44 (BJ18), CD133 (clone 7), Podoplanin (NC-08), CD140a (16A1), CD140b (18A2), Cadherin 11 (16G5), EGFR (AY13), CD340 (24D2), CD146 (P1H12), CD324 (67A4), IgM (MHM-88), CD5 (UCHT2), TCR γ/δ (B1), CD183 (G025H7), CD195 (J418F1), CD32 (FUN-2), CD196 (G034E3), CD185 (J252D4), CD103 (Ber-ACT8), CD69 (FN50), CD62L (DREG-56), CD197 (G043H7), CD161 (HP-3G10), CD152 (BNI3), CD223 (11C3C65), KLRG1 (SA231A2), CD27 (O323), CD107a (H4A3), CD95 (DX2), CD134 (Ber-ACT35 (ACT35)), HLA-DR (L243), CD1c (L161), CD11b (ICRF44), CD64 (10.1), CD141 (M80), CD1d (51.1), CD314 (1D11), CD66b (6/40c), CD35 (E11), CD57 Recombinant (QA17A04), CD366 (F38-2E2), CD272 (MIH26), CD278 (C398.4A), CD275 (9F.8A4), CD58 (TS2/9), CD96 (NK92.39), CD39 (A1), CD178 (NOK-1), CX3CR1 (K0124E1), CD24 (ML5), CD21 (Bu32), CD11a (TS2/4), IgA (HP6123), CD79b (CB3-1), CD66a/c/e (ASL-32), CD244 (C1.7), CD27 (LG.3A10), CD235ab (HIR2), Siglec-8 (7C9), CD206 (15-2), Notch 1 (MHN1-519), integrin β7 (FIB504), CD268 (11C1), CD42b (HIP1), CD54 (HA58), CD62P (AK4), CD119 (GIR-208), IL-10 (JES3-12G8), anti-RORγ (2F7-2), TCR α/β (IP26), Notch 3 (MHN3-21), CD68 (Y1/82A), Rat IgG1, κ isotype Ctrl (RTK2071), Rat IgG1, λ Isotype Ctrl (G0114F7), Rat IgG2a, κ Isotype Ctrl (RTK2758), Rat IgG2c, κ Isotype Ctrl (RTK4174), Armenian Hamster IgG Isotype Ctrl (HTK888), CD102 (CBR-IC2/2), CD106 (STA), CD122 (TU27), CD267 (1A1), CD62E (HAE-1f), KLRG1 (2F1/KLRG1), CD135 (BV10A4H2), FcεRIα (AER-37 (CRA-1)), CD41 (HIP8), CD137 (4B4-1), CD254 (MIH24), CD43 (CD43-10G7), CD163 (GHI/61), CD83 (HB15e), CD357 (108-17), CD59 (p282 (H19)), CD124 (G077F6), CD13 (WM15), CD184 (12G5), CD2 (TS1/8), CD226 (11A8), CD29 (TS2/16), CD303 (201A), CD49b (P1E6-C5), CD61 (VI-PL2), CD81 (5A6), CD98 (MEM-108), IgG Fc (M1310G05), CD177 (MEM-166), IgD (IA6-2), CD18 (TS1/18), CD28 (CD28.2), TSLPR (1D3), CD38 (HIT2), CD127 (A019D5), CD45 (HI30), CD15 (W6D3), CD22 (S-HCL-1), CD71 (CY1G4), B7-H4 (MIH43), CD26 (BA5b), CD38 (HB-7), CD72 (3F3), anti-TMEM119 (A16075D), CD338 (5D3), C5L2 (1D9-M12), CD235a (HI264), CD49a (TS2/7), CD49d (9F10), CD73 (AD2), CD79a (HM47), CD9 (HI9a), TCR Vα7.2 (3C10), TCR Vγ9 (B3), TCR Vα24-Jα18 (6B11), CD133 (S16016B) and CD209 (9E9A8), CD110 (S16017E). Details for TotalSeq™-A BioLegend antibodies are summarized in Supplementary Dataset 12.

Validation

Ki67 and ESR1 stainings were performed by the clinical pathology laboratory of UZLeuven, which strictly adheres to the indication of the College of American Pathologists concerning the verification and validation of antibodies used diagnostic purposes and clinical decision making (Fitzgibbons PL et al Arch. Pathol. Lab. Med. 2014; 138:1432-1443). The non-IVD labelled Ab detecting Ki67 was validated using a series of about 20 different cases of tonsil or appendix to demonstrate consistent and reproducible pattern of staining in the germinal centers of the lymphoid structures. The ESR1 antibody was a CE- and IVD-labelled antibody for which we follow verification procedures as described in the specific ASCO/CAP guidelines for ER, PR and HER2 (Hammond MEH et al. Arch. Pathol. Lab. Med. 2010; 134:e48-e72; Allison KM et al Arch. Pathol. Lab. Med. 2020; 144:545-563; Wolff AC et al. Arch. Pathol. Lab. Med. 2018; 142:1364-1382). Additionally, the clinical pathology laboratory has also ISO 15189 accreditation in accordance with national legislation in Belgium.

PD-L1 stainings: PD-L1 staining was centrally performed by Discovery Life Sciences (formerly QualTek Molecular Laboratories or QML) who were blinded for the patient groups (expander versus non-expander). This staining was validated as an immunohistochemistry

(IHC) assay for PD-L1 (Programmed Cell Death 1 Ligand 1, CD274, B7-H1) using the Merck & Co., Inc (Merck) proprietary mouse monoclonal antibody clone 22C3 on formalin-fixed, paraffin-embedded (FFPE) tissues (Dolled-Filhart M. et. Al., Archives of Pathology & Laboratory Medicine: Nov. 2016, Vol. 140, No. 11, pp. 1259-1266; http://dx.doi.org/10.5858/arpa.2015-0544-OA). This PD-L1 (22C3) IHC assay is used by Merck for all clinical trials involving pembrolizumab and their proprietary checkpoint inhibitors.

CITE-seq: All TotalSeq™-A antibody lots are quality tested for Proteogenomics (i.e., Antibody oligonucleotide conjugates designed to enable the generation of transcriptomic and proteomic data simultaneously, using single cell devices such as 10x Genomics' Chromium and Illumina sequencers) by immunofluorescent staining using flow cytometric analysis. The attached oligomer sequence is confirmed by sequencing. More details are given at www.biolegend.com/en-us/reproducibility, www.biolegend.com/en-us/quality-control and https://www.biolegend.com/en-us/totalseq, or on the TotalSeq™-A Human Universal Cocktail product weblink: https://www.biolegend.com/en-us/products/totalseq-a-human-universal-cocktail-v1-0-20321.

Human research participants

Policy information about studies involving human research participants

Population characteristics	All patients included in this study were female. Clinical and pathological characteristics of all patients are summarized in Supplementary Table 1 for treatment-naive patients who received pembrolizumab prior to upfront surgery, and in Supplementary Table 2 for patients who received neoadjuvant chemotherapy prior to pembrolizumab followed by surgery.
Recruitment	Patients with a non-metastatic operable newly diagnosed primary invasive carcinoma of the breast that was histologically confirmed as ER/PR-negative or ER-positive breast cancer with a primary tumor size >1 cm (measured by any of clinical examination) were included. These patients qualified either directly for surgery (when the tumor was >2cm and/or optimal surgery was feasible) or were scheduled for systemic chemotherapy during 20-24 weeks (when the tumor was <2cm or when optimal surgery was not feasible). An additional condition for patients who received neoadjuvant chemotherapy was that they had clear signs of residual tumor on imaging after 3 months of neo-adjuvant chemotherapy (i.e., estimated residual tumor size of at least 10 mm). Chemotherapy was combined with anti-HER2 therapy if the tumor was HER2-positive. All patients either had TNBC, ER-/PR-/HER2+ tumors or ER+/PR+/-/HER2+/- tumors. Recruitment was non-randomized and done independent of the number of ER-positive or ER/PR-negative patients, and independently of the number of patients being treatment-naïve or receiving prior chemotherapy at the time of inclusion. Potential selection bias mainly affects the cohort of patients receiving neoadjuvant chemotherapy, which have to be treated according to the standard-of-care, but for which tissue availability (tumor size >1cm) at the time of surgery is sometimes not fulfilled. Particularly, - The number of patients with HER2-positive breast cancer is relatively low because these patients receive neoadjuvant chemotherapy plus anti-HER2 therapy, which results in high response rates (complete pathological response) and in general no residual tumour of >1 cm prior to surgery. Therefore, these patients can often not be recruited in a study for which paired biopsies are mandatory. - Similarly, the patient cohort receiving prior chemotherapy is biased for non-responders to neoadjuvant chemotherapy. Indeed, patients with a good response to neoadjuvant chemotherapy have a a tumor size <1cm and are not recruited due to the limited tissue availability. - Patients with an ER-positive BC are more likely to get upfront surgery and are underrepresented in the cohort of patients receiving neoadjuvant chemotherapy. - During recruitment, several industry-sponsored clinical trials involving immunotherapy were initiated within our hospital, and some patients preferred to participate to these trials. This delayed study recruitment (anticipated 1 year of recruitment to 2 years of effective recruitment).
Ethics oversight	The protocol of this single center, open-label, non-randomized study (BioKey) was approved by the local medical ethics committee of the University Hospitals Leuven (S60100). The study was conducted according to EU legislation regarding ethical regulations and was registered online (NCT03197389). All patients provided written informed consent.

Note that full information on the approval of the study protocol must also be provided in the manuscript.

Clinical data

Policy information about clinical studies

All manuscripts should comply with the ICMJE guidelines for publication of clinical research and a completed CONSORT checklist must be included with all submissions.

Clinical trial registration	ClinicalTrials.gov Identifier: NCT03197389
Study protocol	The clinical study BioKey (NCT03197389) was an exploratory investigator-driven, single-center, open-label, non-randomized study phase 0 biomarker study. The aim of the study was exploratory, i.e., to quantify TIL scores across breast cancer subtypes and to monitor changes in TIL scores after one dose of pembrolizumab (with or without prior neoadjuvant hemotherapy). Specifically, for this publication, we collected an additional biopsy before anti-PD1 and during surgery (i.e., on-treatment) and subjected these to single-cell profiling. This additional biopsy and the downstream single-cell analyses were not planned in the original study protocol. A fully detailed study protocol is provided as Supplementary Information. Briefly, patients with a non-metastatic operable newly-diagnosed primary invasive carcinoma of the breast that was histologically confirmed as ER-/PR- or ER+ BC with a primary tumor size >1 cm, measured by any clinical examination, including mammography, ultrasound or magnetic resonance imaging, were included (detailed clinical information for each patient is given in Supplementary Tables 1-2). The study consisted of 2 cohorts. A first cohort involved 39 patients scheduled for upfront surgery. Patients had either triple-negative breast cancer (TNBC), HER2+ (ER-/PR-) or ER+/PR+/- (HER2+/-) BC. A second cohort consisted of 15 patients who received neoadjuvant chemotherapy and who had clear signs of residual tumor on imaging after 3 months of neoadjuvant chemotherapy (i.e., estimated residual tumor size of at least 10 mm). Patients either had TNBC, ER-/PR-/HER2+ tumors or ER+/PR+/-/HER2+/- tumors. Chemotherapy was combined with anti-HER2

therapy if the tumor was HER2+. In both cohorts, a single dose of 200 mg pembrolizumab (Keytruda® or anti-PD1) was delivered prior to surgery in a window-of-opportunity setting. Fresh tumor tissue was collected from these patients before (by needle biopsy) and 7-15 (9±2) days after (by resection) pembrolizumab.

Data collection

All patients received a diagnosis for early breast cancer at the Multidisciplinary Center for Breast Cancer (LMBC) in the University Hospitals Leuven (UZLeuven), Leuven, Belgium. If patients qualified for the study, fresh tumor tissue was collected from patients before and 6-14 days after a single dose of 200 mg pembrolizumab. Biopsies were obtained via diagnostic needle biopsy with either a 14G or 18G needle before pembrolizumab and through surgical resection after pembrolizumab. Biopsies were taken at the University Hospitals Leuven, (Leuven, Belgium) and immediately (within 30 minutes) subjected to single-cell dissociation on ice. The latter was performed at the Laboratory of Translational Genetics (VIB and KULeuven, Leuven, Belgium) which is on the same university campus as the hospital (Gasthuisberg). All subsequent wet-lab experiments were performed at the Laboratory for Translational Genetics. High-throughput sequencing was done on a Illumina NovaSeq housed by the Genomics Core at KULeuven. Data analysis was performed using computational resources and services provided by the VSC (Flemish Supercomputer Center, Belgium at KULeuven). Samples were collected between February 2018 and March 2020. The first patient was included 18 January 2018 and the last patient was included 18 February 2020. The last study visit of the last patient was 31/03/2020.

Outcomes

This is a window-of-opportunity study that exploits the 'window' of time after a breast cancer diagnosis and subsequent surgery in the first cohort of patients, or after neoadjuvant chemotherapy but prior to subsequent surgery in the second cohort of patients. Only a single dose of anti-PD1 is given in this short 'window-of-opportunity'. It is unrealistic to expect a significant effect on tumor shrinkage in such short time window. Also, since the tumor is surgically resected after 1 dose of therapy, outcome measurements, such as relapse-free survival, or response by RECIST are not relevant in this study. The study was therefore designed to study the effect of a single dose of pembrolizumab on the tumor microenvironment, and did not aim to explore treatment response or survival effects following checkpoint immunotherapy.